Climatic Change (2026) 179:66
https://doi.org/10.1007/s10584-026-04153-0

Identifying trend reversals in atmospheric ethane from a multi-site analysis

Marina Friedrich[1,2] · Siem Jan Koopman[1,2] · Yicong Lin[1,2] · Emmanuel Mahieu[3] · Stephan Smeekes[4] · Martine De Mazière[5] · Victoria Flood[6] · Matthias Max Frey[7] · Michel Grutter[8] · James W. Hannigan[9] · Frank Hase[7] · Nicholas Jones[10] · Rigel Kivi[11] · Maria Makarova[12] · Isamu Morino[13] · Isao Murata[14] · Tomoo Nagahama[15] · Justus Notholt[16] · Ivan Ortega[9] · Maxime Prignon[17] · Amelie Ninja Röhling[7] · Dan Smale[18] · Kimberly Strong[6] · Yao Té[19] · Minqiang Zhou[20]

Received: 24 April 2025 / Accepted: 12 March 2026

Abstract
Ethane is the most abundant non-methane hydrocarbon in Earth's atmosphere and acts as an indirect greenhouse gas, influencing the atmospheric lifetime of methane. Therefore, understanding the development of trends and identifying trend reversals in atmospheric ethane is crucial. Ethane abundance is measured at different ground-based stations worldwide using Fourier transform infrared remote sensing techniques. We compile a new dataset comprising 26 ethane time series from the Northern and Southern Hemispheres. We analyze their long-term trends using different econometric techniques capable of handling missing data and strong seasonal components present in the data. The resulting trend patterns are consistent across the different methods, with similar estimated trends at the various stations. In the Northern Hemisphere, the common trend across stations declined from the 1990s to 2005, gradually increased over the next decade, and then resumed a similar downward trajectory from 2015 onward. The estimated trends reveal a pronounced peak around 2014/2015, marking a reversal from an upward to a downward trend.

Keywords Atmospheric ethane · FTIR remote sensing · Nonparametric trend analysis · Kalman filter

1 Introduction

Short-lived climate forcers are broadly divided into methane and non-methane volatile organic compounds (NMVOC) (Szopa et al. 2021). They affect the climate and are often also air pollutants. Ethane is the most abundant NMVOC in the atmosphere, sharing important emission sources with methane, a major greenhouse gas with high global warming potential (Franco et al. 2015). The main sources of ethane are anthropogenic (62% from leakage during production and transport of natural gas, 20% from biofuel combustion),

---

Extended author information available on the last page of the article while methane has both natural and anthropogenic sources (Xiao et al. 2008). Understanding trends in atmospheric ethane is crucial to better constrain the anthropogenic sources of methane, in particular from the oil and gas industry (Franco et al. 2016). The ethane abundance in the atmosphere is measured above many ground-based stations using Fourier transform infrared (FTIR) remote sensing techniques. Therefore, observational data is available for a wide spread of locations all over the world. However, trend patterns have only been analyzed in the literature for a subset of these locations.

Several papers have studied trends in atmospheric ethane. For example, Angelbratt et al. (2011) obtain ethane trends until 2006 from four different stations located in the Northern Hemisphere (NH). Zeng et al. (2012) obtain trend estimates until 2009 from the ethane burden above Lauder and Arrival heights. Franco et al. (2015) analyze the trending pattern observed over the Jungfraujoch measurement station. Franco et al. (2016) analyze ethane trends in North America with the support of model simulations. Lutsch et al. (2020) study 10 ethane time series from the NH until 2018. Friedrich et al. (2020a) investigate ethane trends from four different stations, one of them located in the Southern Hemisphere (SH); three of these end in 2014 and one in 2019. Recently, Maddanu and Proietti (2023) analyze ethane trends from 15 different stations until 2021, three of which are located in the SH. From this strand of the literature, we can see trend patterns emerging, which are common to most of the analyzed data sets. Most of the series obtained from stations in the NH share a similar trend pattern: a steady downward trend until around 2007/2008, followed by a significant upward trend. This trend reversal has been found in Franco et al. (2015), Lutsch et al. (2020), Friedrich et al. (2020a) and Maddanu and Proietti (2023). Subsequently, a slowdown of the upward trend around 2014/2015 has been found for the Jungfraujoch in Friedrich et al. (2020a). This is confirmed for some other NH stations in Maddanu and Proietti (2023), resulting in a second trend reversal that has received less attention in the literature up to this point. The SH stations, however, do not share a clear common trending pattern.

In this paper, we investigate the 2014/2015 trend reversal in a new dataset consisting of updated ethane measurements up to 2023 for a total of 26 stations (five from the SH). To understand the long-term developments of the ethane burden in the atmosphere, we carefully analyze the time trends obtained from each of the 26 stations. Our approach combines three distinct econometric techniques. Since FTIR ethane data display a large fraction of missing observations and a strong seasonal pattern, causing high correlation between data points over time, we adopt econometric methods that have been shown to account for these characteristics (Friedrich et al. 2020b; Maddanu and Proietti 2023). Specifically, we estimate smooth trends nonparametrically as in Friedrich et al. (2020a) to get a first impression of the trend at each station. This nonparametric approach allows us to extract a trend curve without making restrictive assumptions on the shape of the trend. We observe a pronounced peak around 2014/2015 in almost all of the estimated trends from the NH. To further validate this observed pattern, we employ a second method using parametric unobserved components models. The results align with the nonparametric analysis, reinforcing the robustness of our conclusions. The findings are also in line with the previous analysis of the ethane burden above the Jungfraujoch found in Friedrich et al. (2020a) and with results from Maddanu and Proietti (2023). To quantify the increase and subsequent decrease, we proceed by assuming (piecewise) linearity of the trend line. Based on this assumption, we test for a break in the linear trend at each station. If a break is present, we locate it and quantify the uncertainty around the break location. We report slopes (with bootstrap confidence intervals) before and after the break. We find evidence for a break in trend between 2013 and 2016 for almost all stations, with the exceptions of Paramaribo and St. Denis. In the NH, the estimated slope coefficient before the break is positive and ranges from 1.3 to 7.3% per year. After the break, it turns negative with magnitudes ranging from −0.4 to −2% per year. In the SH, there is no overall common pattern.

The remainder of the paper is organized as follows. In Sect. 2, we describe the data used for this study. Section 3 explains our general modeling strategy, while the following Sects. 4–6 go into details about our three approaches and presents their results. Section 7 concludes.

2 The data

We study a new and extended dataset consisting of atmospheric ethane abundances recorded at 26 different measurement stations across the world. The data set consists of 21 series obtained from stations in the Northern Hemisphere (NH) and five from the Southern Hemisphere (SH). As shown in Fig. 1, the stations are located across different latitudes and altitudes. More details on the exact location of the measurement stations are summarized in Table 1. The stations are sorted according to latitude in descending order. Eureka to Sodankyla are considered NH high-latitude stations, Harestua to Tsukuba are NH mid-latitude, and Izaña to Paramaribo NH subtropics and tropics stations. Both stations on La Réunion are categorized as SH subtropics and tropics, Wollongong and Lauder as SH mid-latitude, and Arrival Heights as SH high-latitude stations. We additionally observe that the measurement stations at Zugspitze, Jungfraujoch, Izaña, Mauna Loa, and Altzomoni are high-altitude stations, located higher than 2500 meters above sea level.

The data cover a time span of more than 35 years, with the earliest observations going back to 1986 and the most recent ones obtained in 2023. We work with dry-air mole fractions (DAMF) in parts per billion (ppb) instead of with non-normalized ethane total columns

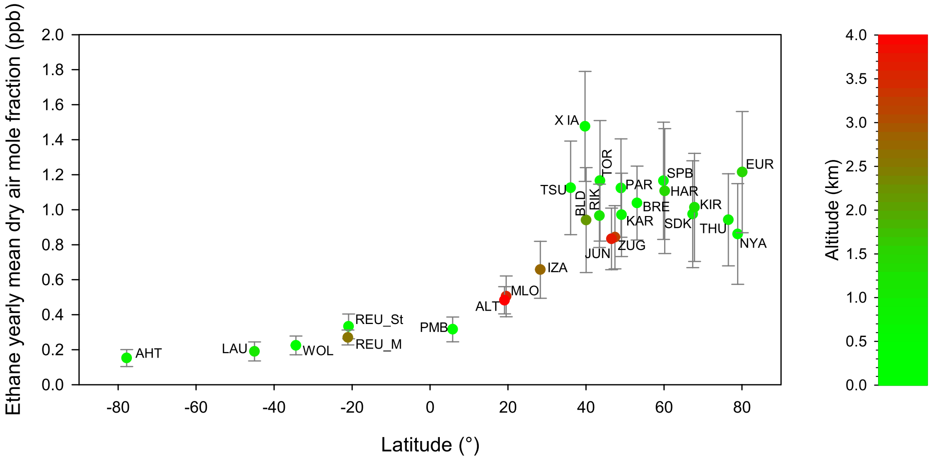

Fig. 1 Latitudinal variation of the ethane yearly mean dry air mole fraction, computed for (the year) 2019 (2018 for Wollongong). The additional effect of altitude is color-coded following the right panel scale. The full names and codes of the stations are listed in Table 1

Table 1 Information on the FTIR measurement stations. Obs. reports the number of days with observations, and the missing percentages are calculated as the number of days without observations divided by the total number of days in the sample range of each station. Stations are sorted according to decreasing latitude for the Northern Hemisphere and increasing latitude for the Southern Hemisphere

Station	Code	Country	Location	Altitude	Range	Obs.	Missing	Reference
Northern Hemisphere								
Eureka	EUR	Canada	80.05°N, 86.42°W	610 m	2006–2020	828	83.40%	Batchelor et al. (2009)
Ny-Ålesund	NYA	Norway	78.92°N, 11.93°E	15 m	1993–2022	882	90.88%	
Thule	THU	Greenland	76.52°N, 68.77°W	225 m	1999–2022	1,537	81.71%	Hannigan et al. (2009)
Kiruna	KIR	Sweden	67.80°N, 20.40°E	420 m	1996–2022	1,962	79.85%	Blumenstock et al. (2009)
Sodankylä	SDK	Finland	67.37°N, 26.63°E	188 m	2012–2023	1,193	70.82%	Kivi and Heikkinen (2016)
Harestua	HAR	Norway	60.2°N, 10.8°E	596 m	1994–2021	1,224	87.62%	
St. Petersburg	SPB	Russia	59.88°N, 29.83°E	20 m	2009–2022	912	81.69%	Makarova et al. (2024)
Bremen	BRE	Germany	53.10°N, 8.80°E	27 m	2004–2022	548	91.85%	
Karlsruhe	KAR	Germany	49.1°N, 8.42°E	110 m	2010–2022	1,162	73.85%	Kiel et al. (2016)
Paris	PAR	France	48.97°N, 2.37°E	60 m	2011–2022	551	86.45%	
Zugspitze	ZUG	Germany	47.25°N, 10.59°E	2,964 m	1995–2023	2,564	74.82%	Hausmann et al. (2016)
Jungfraujoch	JUN	Switzerland	46.55°N, 7.98°E	3,580 m	1986–2022	3,174	76.39%	Zander et al. (2008), Franco et al. (2015)
Toronto	TOR	Canada	43.66°N, 79.40°W	174 m	2002–2022	2,377	67.78%	Yamanouchi et al. (2023)
Rikubetsu	RIK	Japan	43.46°N, 143.77°E	380 m	1995–2022	1,078	89.10%	
Boulder	BLD	United States	39.99°N, 105.26°W	1,634 m	2010–2021	973	79.07%	Ortega et al. (2019)
Xianghe	XIA	China	39.75°N, 116.96°E	46 m	2018–2021	706	45.52%	Zhou et al. (2023)
Tsukuba	TSU	Japan	36.05°N, 140.12°E	31 m	2001–2022	1,107	85.94%	
Izaña	IZA	Spain	28.30°N, 16.50°W	2,367 m	1999–2022	2,309	73.31%	García et al. (2021)
Mauna Loa	MLO	United States	19.54°N, 155.58°W	3,397 m	1995–2022	2,957	70.30%	Hannigan et al. (2009)
Altzomoni	ALT	Mexico	19.12°N, 98.65°W	3,985 m	2012–2023	1,176	69.44%	Baylon et al. (2017)
Paramaribo	PMB	Suriname	5.74°N, 55.2°W	23 m	2013–2022	102	96.89%	
Southern Hemisphere								

Table 1 (continued)

Station	Code	Country	Location	Altitude	Range	Obs.	Missing	Reference
La Réunion, St. Denis	REU_ST	France	20.9°S, 55.5°E	85 m	2004–2015	745	81.15%	Vigouroux et al. (2012)
La Réunion, Maïdo	REU_M	France	21.1°S, 55.4°E	2,155 m	2013–2019	1,095	56.08%	
Wollongong	WOL	Australia	34.24°S, 150.52°E	30 m	2007–2020	2,324	52.48%	Griffith et al. (2021)
Lauder	LAU	New Zealand	45.04°S, 169.68°E	370 m	1996–2022	3,504	63.56%	Zeng et al. (2012)
Arrival Heights	AHT	Antarctica	77.83°S, 166.67°E	184 m	1997–2022	1,170	87.61%	Zeng et al. (2012)

expressed in the number of molecules per cm^2. The DAMF corresponds to the ratio between the actual total column of the target gas, here ethane, and the dry-air pressure column. The way to compute DAMF is provided, e.g., in Pardo Cantos et al. (2022, see Eq. (2) in Sect. 4.3.1). Whenever multiple measurements are taken on one day, we consider daily averages.

The last column of Table 1 shows the percentage of missing data per station. They are obtained as the number of days in the sample period of the respective station in which no observations are available. With 45.52% of missing observations, the series obtained at Xianghe, China, contains the highest ratio of observations, while the Paramaribo series has the highest ratio of missing data with 96.89% (although there are still 102 observations available). Several limiting factors can explain significant fractions of missing data. The most important one is weather conditions since the ground-based FTIR technique requires a cloud-free sky to record spectra. Other unfavorable circumstances include instrumental failures and campaign-type observations, which are generally limited in duration. These percentages clearly indicate that missing data is a severe and non-negligible problem in our analysis. In particular, common imputation techniques such as linear interpolation are likely to be imprecise and may introduce strong biases into the outcomes. Therefore, we do not impute the data but use statistical methods that allow for missing values. A strong seasonal pattern further characterizes the data, as ethane degrades faster under warm weather conditions than in cold temperatures, and therefore, the measurements display local peaks every winter period. The seasonal pattern is clearly visible in Fig. 2, which plots a subset of six series. From the NH, we select one mid-latitude station (Harestua), two mid-latitude stations - one of which is a high altitude (Jungfraujoch) and the other one a low altitude station (Karlsruhe) – as well as one station from the subtropics and tropics (Paramaribo). From the SH, we select one mid-latitude (Lauder) and one high-latitude station (Arrival Heights). Even though the displayed data have different sample lengths, the differences in data availability are visible. Lauder is the most complete among this subgroup with 64% of missing data, while Paramaribo is the most incomplete with almost 97% of missing data. As in Fig. 2, we see that the overall burden is lower in the SH than in the NH and gets lower with decreasing latitude. Comparing the NH mid-latitude stations Jungfraujoch and Karlsruhe, we observe an expected lower average burden for the high-altitude station due to the altitude difference. Commonalities in long-term behavior over time are, however, not evident from these plots due to the strong seasonality and missing observations. In the next section, we proceed with the extraction of long-term trends using statistical techniques.

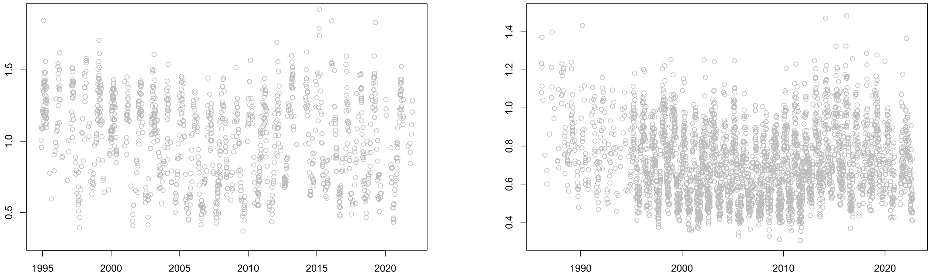

(a) Harestua (b) Jungfraujoch

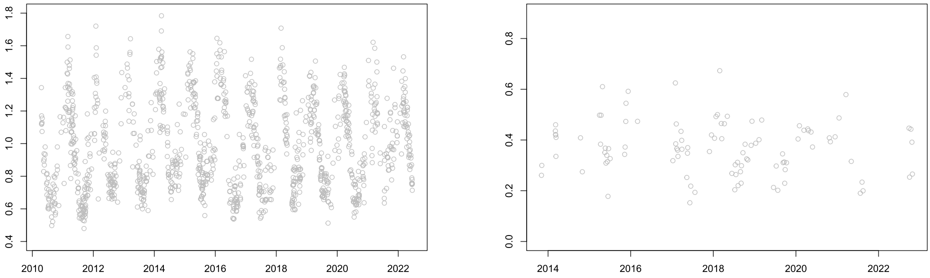

(c) Karlsruhe (d) Paramaribo

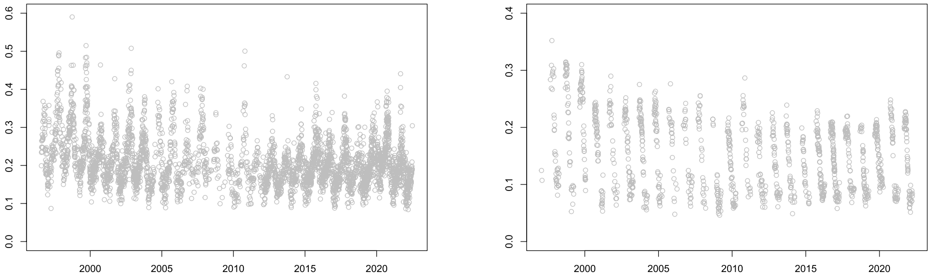

(e) Lauder (f) Arrival Heights

Fig. 2 Temporal development of ethane DAMF data in ppb obtained from different measurement stations. Note that the length of the sample differs for each station, which can make the seasonality and data availability appear more or less dense

3 A general set-up for long-term trend modeling

The trending behavior of ethane abundance may consist of long-run movements, seasonal fluctuations, and short-run variations. Hence, we consider the model

$$y_t = \mu_t + \psi_t + \varepsilon_t, \qquad t = 1, \ldots, T, \tag{1}$$

where y_t denotes the ethane abundance measured at a given station at day t, the variable μ_t represents the long-run trend component over years, which is the primary focus of our analysis, variable ψ_t captures seasonal effects within each year, and ε_t is a stochastic error term that accounts for short-run fluctuations in y_t. The technical statistical details of the different approaches are discussed below.

To draw solid conclusions about the trending behaviors of ethane abundance, we focus on the treatment of the trend component μ_t and remove the seasonal component ψ_t from the ethane time series y_t. In other words, we seasonally adjust the data a priori, which is a standard procedure in official statistics, for example, see https://www.census.gov/data/software/x13as.html (last accessed on August 22, 2025). In this study, we analyze daily ethane measures and adopt the unobserved components time series model (UCTSM) for seasonal adjustment, see Appendix A.2. In Harvey et al. (1997) it is argued that the challenges of seasonal adjustment of weekly or daily data can be most effectively addressed within the UCTSM framework. The UCTSM requires both components to be specified as latent random processes. For example, the trend can be modeled as a random walk process, and the seasonal can be modeled as a stochastic Fourier process, see also the discussion in Proietti (2000). Once the model is formulated in state space form, the Kalman filter and related methods are adopted to estimate the unknown parameters by maximum likelihood, and to extract the components μ_t and ψ_t using a smoothing method, see Durbin and Koopman (2012). The seasonal adjustment is achieved by simply subtracting the estimate of ψ_t from the data.

The trend component μ_t in this study is treated by different statistical approaches, each with a distinct perspective. These methods may involve nonparametric or parametric models, and the trend itself may be specified as either a deterministic or a random process. First, following Friedrich et al. (2020a), we assume that the trend μ_t is a deterministic yet fully unknown function of time, and we estimate it nonparametrically. Second, we can extract the trend from the UCTSM model that is used for the seasonal adjustment of the data. Third, to achieve a more structural interpretation of the trend and understand its rate of change, we assume piecewise linearity and employ a parametric broken linear trend approach (Perron and Zhu 2005, Friedrich et al. 2020a, Beutner et al. 2023). This method enables us to calculate the rates of increase and decrease both before and after the peak.

4 Nonparametric trend analysis

To gain an initial understanding of the long-term trend μ_t in Eq. (1), we first consider a nonparametric specification that imposes minimal assumptions on the form of the trend. Specifically, let

$$\mu_t = g(t/T), \qquad t = 1, ..., T, \tag{2}$$

where $g(\cdot)$ denotes a smooth (i.e., twice continuously differentiable) unknown function defined on the interval $[0, 1]$. As is standard with this approach, we map all time points into the interval $[0, 1]$ by dividing by T. This results in a theoretically consistent approximation of g with increasingly dense observations in the interval $[0, 1]$ as T increases (see, e.g., Robinson 1989; Cai 2007). This is mainly done for theoretical purposes and does not affect estimation in practice. Apart from the smoothness assumption, we do not need to restrict the functional form of the trend.

Our main goal is to estimate the function $g(\cdot)$ and quantify the uncertainty around this estimate, as it reflects the long-term trending behavior of ethane abundance. We apply the toolkit proposed in Friedrich et al. (2020a, 2020b), employing a nonparametric kernel estimator in combination with the autoregressive wild bootstrap (AWB) to construct confidence bands. The estimator requires a smoothing parameter known as the bandwidth $h > 0$. The choice typically depends on the context of the study, but data-driven procedures can assist with this selection. A common approach for time series data is the Modified Cross-Validation (MCV) approach proposed by Chu and Marron (1991), which has been adopted, for instance, in Friedrich et al. (2020a). Given the substantial amount of missing values in several records (see Table 1) and the fact that some time series, such as Xianghe, are relatively short, selecting an optimal bandwidth for each series individually is challenging or even infeasible. At the same time, the smoothness of ethane abundance can reasonably be expected to be comparable across stations within the same hemisphere, as emissions may be influenced by common regional drivers. For this reason, we pool the time series within each hemisphere and determine a single bandwidth per hemisphere, which allows shorter records to “borrow” information from surrounding stations. This approach ensures a common level of smoothness within hemispheres and thereby also facilitates comparisons between trends. Importantly, however, adopting a common h does not imply that the trends themselves must evolve in the same direction or exhibit the same magnitude. For this purpose, the MCV approach is adapted to account for multiple time series, with the technical details provided in Appendix A. In our case, a bandwidth of $h = 0.09$ is selected by the criterion for the NH and $h = 0.125$ for the SH.

Figure 3 displays the nonparametric trend estimates and 95%-level confidence bands. The stations are sorted according to latitude in descending order. The DAMF are plotted as grey circles, the black line is the estimated trend line, and the blue lines are the confidence bands. Overall, the nonparametric trend estimates capture the movement of ethane abundance at each station well.

To examine potential co-movements, we demean all estimated trend curves and plot them together in Fig. 4. Panel (a) includes all stations from the Northern Hemisphere, and panel (b) all Southern Hemisphere. We find a pronounced peak around 2014/2015 for almost all series of the NH. For series that start early (e.g., Harestua, Rikubetsu, Jungfraujoch, Zugspitze), we additionally see an overall downward trend until around 2006–2009 – interrupted by a local peak around 1998 and 2002 (Yurganov et al. 2004, 2005) – which then turns into an upward trend until the 2014/2015 peak. It is important to emphasize the common tendency observed across the NH stations. The common trend declined from the 1990s until around 2005. After that, it gradually increased for about 10 years. This downward-upward trend reversal has been associated in the literature with an increasing shale gas exploitation in the United States (Franco et al. 2015; Friedrich et al. 2020a; Maddanu and Proietti 2023). However, starting in 2015, the trend began to decline again at a pace similar to that seen in the 1990s. This latest trend reversal has been tentatively attributed to the evolution of the crude oil price which showed a severe reduction as of 2015 (Friedrich et al. 2020a; Angot et al. 2021; Maddanu and Proietti 2023). This affected the profitability of fracking, possibly leading to a rapid reduction of related emissions, given the versatility of the U.S. industry and economy.[1] It is interesting to note that Zhang et al. (2024) found that the trend in the eth-

---

[1] In line with Franco et al. (2016) and Maddanu and Proietti (2023), we examine the correlation between the trend reversals identified by our nonparametric and parametric models and U.S. crude oil production as well

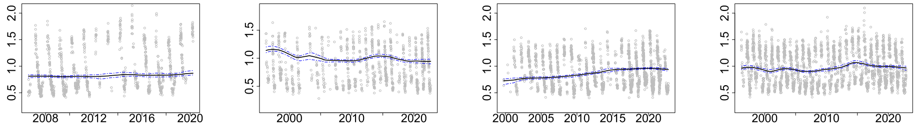

(a) Eureka (b) Ny-Alesund (c) Thule (d) Kiruna

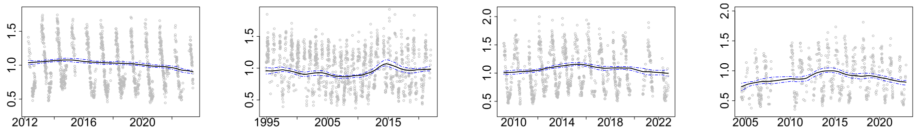

(e) Sodankyla (f) Harestua (g) St. Petersburg (h) Bremen

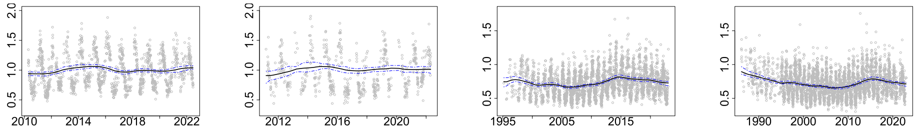

(i) Karlsruhe (j) Paris (k) Zugspitze (l) Jungfraujoch

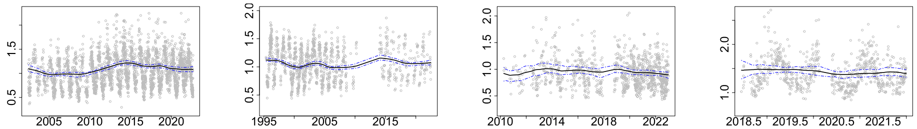

(m) Toronto (n) Rikubetsu (o) Boulder (p) Xianghe

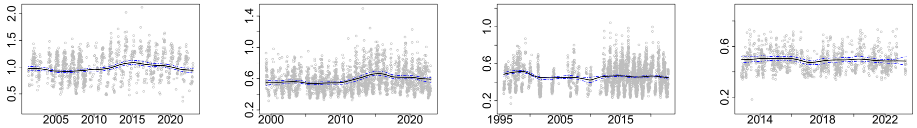

(q) Tsukuba (r) Izana (s) Mauna Loa (t) Altzomoni

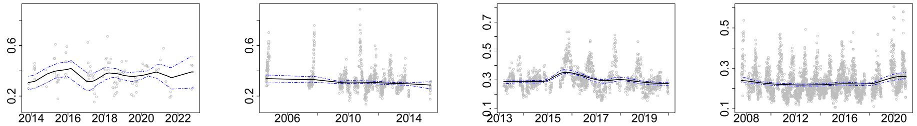

(u) Paramaribo (v) REU - St. Denis (w) REU - Maido (x) Wollongong

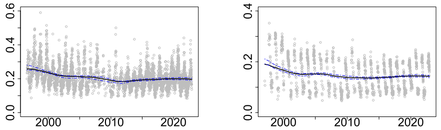

(y) Lauder (z) Arrival Heights

Fig. 3 Nonparametric trend results for all stations. Dry-air mole fractions (in ppb) are represented by the grey circles, the trend estimate by the black line (with bandwidths $h=0.09$ for NH and $h=0.125$ for SH), and the blue lines indicate the 95% confidence bands

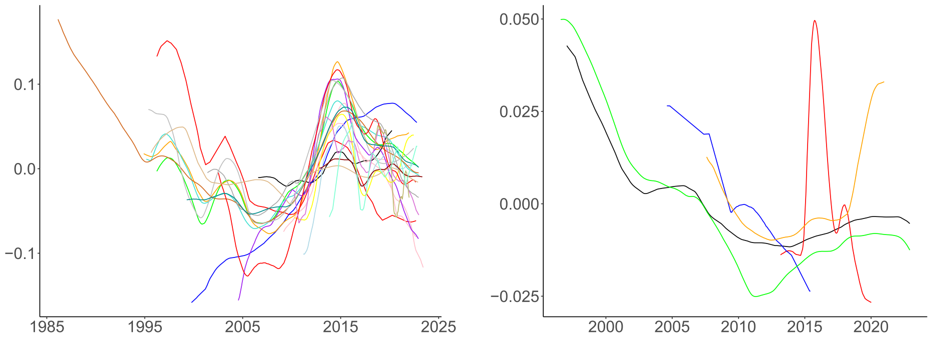

(a) Northern Hemisphere, Nonparametric (b) Southern Hemisphere, Nonparametric

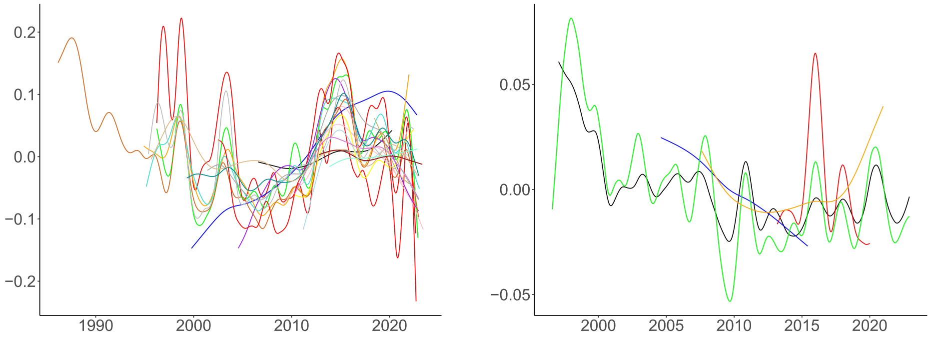

(c) Northern Hemisphere, UCTSM (d) Southern Hemisphere, UCTSM

Fig. 4 Demeaned trend lines for all stations to compare comovements. Panels (**a**) and (**b**) show the nonparametrically estimated trends, while panels (**c**) and (**d**) show the estimated UCTSM trends for the Northern (left panels) and Southern Hemisphere (right panels). Note that in the left panels, the brown lines represent the estimated trends for Jungfraujoch, which is the longest time series shown

ane emissions was decoupled from ethane production, based on observations performed in the U.S. by the National Oceanic and Atmospheric Administration (NOAA) Global Monitoring Laboratory. Indeed, they report that US emissions would have risen by 0.25 ± 0.31 Tg over 2015–2020 while reported ethane production increased by 78%. These authors provide several ways to explain this decoupling, including the exploitation of new wells with lower ethane content, and/or that leakage at the various phases of production (drilling, storage, transport) may have diminished Zhang et al. (2024).

The 2014/2015 peak stands out as it appears across nearly all series in the NH. Exceptions include Xianghe, which started only in 2018, and Mauna Loa, which had multiple large gaps before the period of interest, complicating the accurate estimation of the long-term trend during this time. For the other series, we will further analyze the characteristics of the observed peak and the resulting trend reversal in the remaining two sections.

We also observe that the SH exhibits less distinct common trends. However, we see a downward-upward trend reversal for some locations, where early data is available. The reversal is estimated to happen between 2010 and 2015, which is later than in the NH. This

---

as U.S. natural gas gross withdrawals in Appendix B.

could imply a delayed effect of the shale gas extraction in the SH compared to the NH. Specifically, there is a common downward trend visible for Lauder and Arrival Heights where observations are available before 2000. For Wollongong and La Réunion St. Denis, the downward trend is also visible, even though the observations start a bit later.

5 State-space modeling of trends

A parametric approach to trend estimation can be based on an unobserved components time series model (UCTSM) that includes a trend component. We have discussed the UCTSM in Sect. 2 for the purpose of seasonal adjustment, given that the data from all stations are subject to year-on-year (trend) and within-year (seasonal) changes. We therefore adopt a state-space approach based on the decomposition in Eq. (1) in Sect. 3, with a long-term trend component μ_t and a seasonal effects component ψ_t. We treat these components as unobserved dynamic processes and include them jointly in the UCTSM; see Durbin and Koopman (2012). We have found that the trend component μ_t in Eq. (1) can appropriately be specified as a smooth stochastic trend function, represented by an integrated random walk process. Hence, the role of μ_t is to account for the low-frequency year-on-year dynamics in the time series y_t. Furthermore, the seasonal within-year component ψ_t has shown to be effective when it is treated as a sum of S stochastically time-varying Fourier series corresponding to the seasonal frequencies $2\pi j \,/\, 365.25$, with $j = 1, 2, 3$.

More specific details of the statical specifications of the trend and seasonal components, and the methodology to estimate the model parameters and to extract the trend component, are reviewed in Appendix A.2. A convenient feature of the state-space statistical treatment is that missing observations, of which there are many in our data set, are treated as an integrated part of the analysis.

5.1 Trend estimation results based on UCTSM

We apply the UCTSM framework to the ethane dry-air mole fractions. The results are plotted in Fig. 5. Each plot contains the original data, the corresponding trend component estimate, and the 95%-level confidence interval. The start and end of each time series plot can be different as the data availability for each station varies. Although there are commonalities to be found in the trend estimates, they can also be quite different among the different stations. Most trend estimates of the SH stations have wider confidence intervals due to the shorter samples with larger amounts of missing values. Furthermore, the five estimated SH trends have lower values compared to most of the estimated NH trends. The estimated trends of the stations are jointly presented in Fig. 4, the NH trends are presented in the left panel and the SH trends in the right panel. NH trends show some common patterns. Many NH trend estimates show increasing behavior between 2008 and 2015 or at least show upward trends in many of their sub-samples during this period. However, most stations show a downward trend after 2014/15. The trend of Thule stands out with a strong increasing pattern from 2000 onward. The trends from the SH stations do not provide a clear common pattern. The trend of Wollongong stands out with a strong increasing pattern from 2014 onward. To facilitate further comparisons, also between the trends of the nonparametric method and the

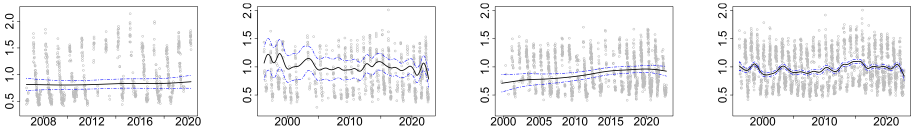

(a) Eureka (b) Ny-Alesund (c) Thule (d) Kiruna

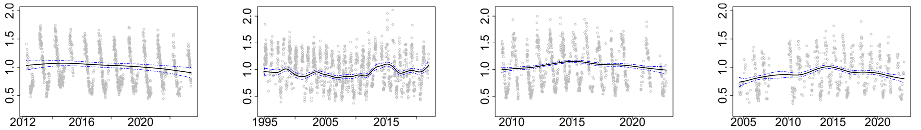

(e) Sodankyla (f) Harestua (g) St. Petersburg (h) Bremen

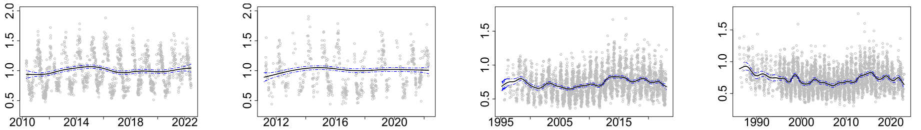

(i) Karlsruhe (j) Paris (k) Zugspitze (l) Jungfraujoch

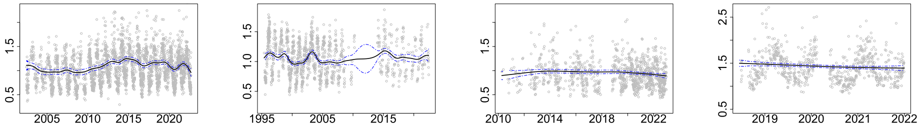

(m) Toronto (n) Rikubetsu (o) Boulder (p) Xianghe

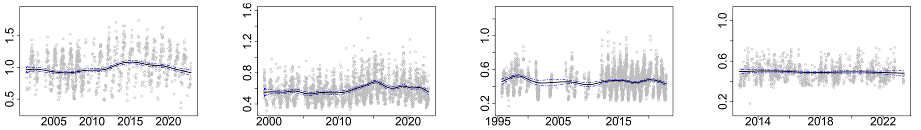

(q) Tsukuba (r) Izana (s) Mauna Loa (t) Altzomoni

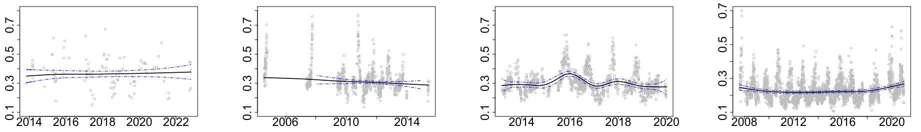

(u) Paramaribo (v) REU - St. Denis (w) REU - Maido (x) Wollongong

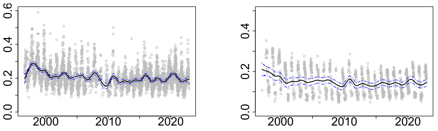

(y) Lauder (z) Arrival Heights

Fig. 5 Estimated UCTSM trends results for all stations. Dry-air mole fractions (in ppb) are given as grey circles, the trend estimate by the black line and the blue lines indicate the 95% confidence intervals

UCTSM framework, we present in Fig. B1, in Appendix B, the yearly means of the trend estimates from both approaches.

Note that the error process of this model is assumed to be independent, which distinguishes it from the other approaches used in this paper. To also assess the validity of this assumption, we examine the residuals from this model in Appendix B. For most stations, the residual autocorrelation is low, although some exceptions are observed. These cases could potentially be addressed by allowing for long-memory behavior in the cyclical component or by introducing a correlated error structure. We leave these extensions for future research, as they are not expected to materially affect the shape of the estimated long-term trends.

5.2 Trend breaks in 2014–2016 and percentage changes

To identify the most recent breaks in the trend estimates (in most cases, breaks in the years 2014–2016), we focus on the trend-slope estimates to detect the dates of the breaks. It can be observed that when the trend-slope component is negative, the trend is decreasing, and when the trend-slope is positive, the trend is increasing. Hence, when the trend-slope component switches its sign over time (its value is then close to zero when dealing with sufficiently smooth trends), the trend component shows a break from an increasing trend towards a decreasing trend (or vice versa). Therefore, the location of a break in the trend can be traced via the trend-slope estimate (at the position where it crosses the zero-line). When we locate the most recent zero-valued trend-slope estimate, we obtain the dates as presented in Table 2. We can interpret these dates as indicative of when the break has taken place.

For many stations, no trend breaks can be detected because they are overall decreasing or increasing (no zero values found in the slope estimate). In cases where the trend is estimated as a fixed trend line, then no break is detected. When a break is identified, we measure the change in the trend level over the subsequent five years. Specifically, we report the percentage change in the trend value five years after the break date, given by

$$\%\mathrm{TrendChange} = 100 \times \frac{\mathrm{TrendValue}_{\mathrm{breakdate+5years}} - \mathrm{TrendValue}_{\mathrm{breakdate}}}{\mathrm{TrendValue}_{\mathrm{breakdate}}}.$$

The results in Table 2 indicate that for 8 out of 21 stations in the NH, we have not detected a break in the trend in the last 7–8 years of the sample. Most of the 15 break dates for the NH and SH stations occur either late in 2014 or in 2015, while the ones for Zugspitze and Boulder occur earlier in 2014, and for Wollongong, the (positive) break occurs in early 2016. All trend changes in the NH are negative, which implies that all trends decrease after the break dates. The only (slight) negative break detected within the five SH stations is for Maïdo, while the one for Wollongong is a positive break, implying an increasing trend after 17 February 2016. For the NH stations, the largest trend changes of 7% and higher are detected for the stations Ny-Ålesund, Kiruna, St. Petersburg, Bremen, Jungfraujoch, Toronto, and Tsukuba, while trend changes closer to $3-5\%$ are obtained for Sodankylä, Kalsruhe, and Zugspitze.

Table 2 Estimated ethane trend break points around 2015 and percentage trend change after five years, based on the UCTSM analysis

	Break Date			
Station	Year	Month	Day	% Trend Change
Northern Hemisphere				
Eureka	-	-	-	-
Ny-Ålesund	2014	9	25	−7.397
Thule	-	-	-	-
Kiruna	2015	7	23	−11.95
Sodankylä	2014	9	22	−5.609
Harestua	-	-	-	-
St. Petersburg	2015	2	23	−7.886
Bremen	2014	6	29	−10.22
Karlsruhe	2015	1	13	−5.881
Paris	2014	11	18	−0.289
Zugspitze	2014	4	30	−3.308
Jungfraujoch	2015	6	26	−15.01
Toronto	2014	10	22	−8.284
Rikubetsu	2015	4	24	−2.563
Boulder	2014	2	2	−1.581
Xianghe	-	-	-	
Tsukuba	2015	2	7	−7.400
Izaña	-	-	-	-
Mauna Loa	-	-	-	-
Altzomoni	-	-	-	-
Paramaribo	-	-	-	-
Southern Hemisphere				
REU St. Denis	-	-	-	-
REU Maïdo	2015	12	24	−0.240
Wollongong	2016	2	17	2.081
Lauder	-	-	-	-
Arrival Heights	-	-	-	-

6 Direct approach to modeling trend breaks

The UCTSM framework discussed in Sect. 5 indicates that many stations exhibit a trend break in 2015. In this section, we carry out a structural analysis using the well-known broken linear trend model, originally proposed by Perron and Zhu (2005). For related asymptotic results, see Harvey and Leybourne (2014) and Beutner et al. (2023). Specifically, we assume that the trend follows a piecewise linear shape and define μ_t as follows:

$$\mu_t = \alpha + \beta t + \delta D_{t,T_1}, \tag{3}$$

where $D_{t,T_1} = 0$ for $t \leq T_1$, and $t - T_1$ otherwise, with T_1 denoting the unknown break location. Eq. (3) describes a broken trend model with an unknown break point at T_1. The intercept and slope parameters before the break are α and β, respectively. For $t > T_1$, the dummy variable D_{t,T_1} induces a change *solely* in the slope coefficient from β to $\beta + \delta$, while maintaining the intercept to exclude a jump in trend at the break date. This prevents the modeled ethane concentration from exhibiting unrealistic behavior at $t = T_1$. For the specification of the seasonal component ψ_t, we again adopt the Fourier series as in the previous sections (see Eq. (A10)).

The parameters of interest are (α, β, δ), the parameters in the Fourier specification, and the unknown break date T_1. We first test for the presence of a break using the test statistic F_T given in Friedrich et al. (2020a), Eq. (3.3), which compares the sum of squared residuals of a model without break to the lowest sum of squared residuals of a model including one break. Critical values for the test are obtained with the AWB. Given a significance level of the test, the critical value of the test determines the cutoff point. If the test indicates evidence of a break, we estimate its location and obtain confidence intervals as in Friedrich et al. (2020a). We again use the autoregressive wild bootstrap for obtaining confidence intervals, as it has been theoretically shown to correctly mimic the missing data and variance patterns.

Since we want to focus on the 2014/2015 trend reversal pattern and the existing approach only allows for one trend break, we have to restrict the longer series to be able to capture our break point of interest. To this end, we disregard the data collected before 2004 in this analysis. The estimated break locations, slope coefficients, and confidence intervals obtained with the AWB are given in Table 3 for the NH and Table 4 for the SH. If a break is detected by the test, the tables report the estimated slope coefficients $\hat{\beta}$ before the break and $\hat{\beta} + \hat{\delta}$ after the break. If no break is detected, the overall slope coefficient $\hat{\beta}$ is reported. The test results are reported in Table B1 in Appendix B.

The broken linear trend lines are plotted in Fig. 6. The dry-air mole fraction data are plotted as grey circles. Furthermore, the seasonal fit is given by the black line, and the blue line shows the (broken) trend line. In cases where a break is present, the two dotted vertical lines show the confidence intervals around the break location corresponding to the results in Tables 3 and 4. In cases where no break is found by the test, only the trend line is displayed.

Several key observations can be made based on Tables 3 and 4 and Fig. 6. First, we find evidence for a break in trend at a 10% significance level for almost all stations, with the exceptions of Eureka, Altzomoni, and Paramaribo in the NH and St. Denis in the SH. Second, if there is evidence for a break at an NH station, it is mostly located between 2013 and 2016, with confidence intervals spanning 2013 until 2020 in the widest case (Boulder).[2] We note first that we employ a trim fraction of 0.1 at both the beginning and the end of the sample, as is standard in the literature for valid structural break tests (see also $\lambda = 0.1$ in the notation of Friedrich et al. (2020a)). After trimming, such a situation typically arises either when no structural break is present or when a break exists but its magnitude is too small to be accurately identified, in which case the confidence intervals may span the entire trimmed sample and the estimated break date (if any) may lie at the beginning or the end of the sample, depending on the data. Two exceptions are Thule and Mauna Loa, with late breaks occurring in 2019 and 2021. Third, the estimated slope coefficient before the break is positive and negative after the break in the NH. The corresponding 95% confidence intervals indicate that all pre-break slope estimates are significantly different from zero. The post-break slopes of Paris and Zugspitze are the only ones that are not significantly different from zero. The estimated slopes range from 0.8 to 8.8% per year before the break. After the break, they vary from −0.4 to −2.2% per year. Fourth, in the SH, the common pattern is less clear. La Réunion Maïdo and Arrival Heights share the NH pattern, with a break around 2015 and

---

[2] Note that for Boulder, the lower bound of the confidence interval for the break location coincides with the estimated break date.

Table 3 Point estimate and 95% confidence interval [CI] of the break date T_1 as well as the slope parameter β before and after the break in cases where we find evidence of a break in the time series, otherwise the overall slope is reported

Individual break dates and parameter estimates for the NH					
Station	Break	[CI]	Period	Slope (%)	[CI] (%)
Eureka	-	-		0.34	[0.18, 0.51]
Ny-Ålesund	2015.24	[2013.73,2016.60]	*before*	0.83	[0.55, 1.10]
			after	−1.41	[−1.81, −0.99]
Thule	2019.64	[2018.75,2020.24]	*before*	1.41	[1.31, 1.52]
			after	−1.60	[−2.24, −1.03]
Kiruna	2015.40	[2014.23, 2016.35]	*before*	1.58	[1.37, 1.81]
			after	−1.25	[−1.63, −0.88]
Sodankylä	2014.85	[2014.21,2015.43]	*before*	2.16	[1.24, 3.05]
			after	−1.78	[−2.02, −1.55]
Harestua	2015.19	[2012.78,2017.12]	*before*	1.71	[1.28, 2.12]
			after	−0.90	[−1.58, −0.24]
St. Petersburg	2015.09	[2014.57,2015.64]	*before*	2.95	[2.51, 3.41]
			after	−2.09	[−2.47, −1.69]
Bremen	2014.61	[2013.75,2015.63]	*before*	2.43	[2.07, 2.80]
			after	−2.16	[−2.58, −1.72]
Karlsruhe	2013.90	[2013.11,2015.20]	*before*	3.47	[2.50, 4.47]
			after	−0.53	[−0.90, −0.17]
Paris	2013.13	[2012.39,2014.58]	*before*	8.80	[4.82, 11.5]
			after	−0.37	[−0.87, 0.11]
Zugspitze	2015.40	[2014.44,2016.25]	*before*	1.67	[1.46, 1.86]
			after	−1.17	[−1.49, 0.84]
Jungfraujoch	2015.65	[2014.59,2016.75]	*before*	1.52	[1.31, 1.72]
			after	−1.19	[−1.57, −0.81]
Toronto	2014.86	[2014.01,2015.67]	*before*	2.89	[2.55, 3.24]
			after	−1.86	[−2.34, −1.33]
Rikubetsu	2015.15	[2014.02,2017.20]	*before*	1.48	[1.14, 1.81]
			after	−1.18	[−1.81, −0.53]
Boulder	2013.62	[2013.62,2020.40]	*before*	4.46	[1.22, 7.48]
			after	−1.04	[−1.61, −0.50]
Tsukuba	2016.13	[2015.02,2016.92]	*before*	1.54	[1.32, 1.78]
			after	−2.06	[−2.60, −1.53]
Izaña	2015.50	[2014.24,2016.51]	*before*	1.37	[1.18, 1.57]
			after	−0.93	[−1.23, −0.64]
Mauna Loa	2021.37	[2019.86,2021.86]	*before*	0.126	[0.04, 0.21]
			after	−2.61	[−28.88, −1.74]
Altzomoni	-	-		−0.16	[−0.30, −0.02]
Paramaribo	-	-		0.24	[−0.38, 0.92]

an upward-downward trend pattern. La Réunion St. Denis shows a significant downward trend and no evidence for a break. Note that the La Réunion stations are located in close proximity but have little time overlap. Specifically, measurements at St. Denis end in 2015, while the time series at Maïdo begins in 2013. Wollongong and Lauder show a downward-upward trend reversal between 2011 and 2017, similar to the early trend reversal in the NH.

Table 4 Point estimate and 95% confidence interval [CI] of the break date T_1 as well as the slope parameter β before and after the break in cases where we find evidence of a break in the time series, otherwise the overall slope is reported

Individual break dates and parameter estimates for the SH

Station	Break	[CI]	Period	Slope (%)	[CI] (%)
La Réunion St.Denis	-	-		−0.47	[−0.64, −0.29]
La Réunion Maido	2015.87	[2015.58,2016.27]	*before*	2.54	[2.04, 3.04]
			after	−1.80	[−2.09, −1.50]
Wollongong	2017.66	[2017.10,2019.72]	*before*	−0.10	[−0.18, −0.04]
			after	1.53	[1.16, 1.86]
Lauder	2011.84	[2009.63,2013.86]	*before*	−0.36	[−0.45, −0.27]
			after	0.13	[0.07, 0.20]
Arrival Heights	2014.61	[2013.75,2015.36]	*before*	2.43	[2.07, 2.80]
			after	−2.16	[−2.58, −1.72]

This could again speak for a delayed effect of shale gas extraction in the SH. Figure 4 is in line with the observed break results.

7 Conclusion

We analyzed a new dataset of atmospheric ethane abundance measured at 26 stations around the globe. We assessed the trend patterns for each time series using three distinct statistical approaches. These approaches have been selected because of their ability to handle the large fraction of missing observations, autocorrelation as well as heteroskedasticity in the data. The first two methods, namely the nonparametric and UCTSM approaches, revealed that ethane trends in the Northern Hemisphere show similar patterns. Specifically, both approaches identified a peak and subsequent trend reversal from upward to downward around 2014/2015, with the NH trend declining from the 1990s to 2005, rising for the next decade, and then declining again at a similar pace from 2015 onward.

To further investigate this trend reversal, we applied a broken linear trend model in two steps. First, we conducted a formal break test to determine whether a linear trend or a linear trend with one break provides a better fit to the data. Next, we estimated the (broken) trend model and reported the slope estimates, which indicate the annual percentage change. Our findings indicate that nearly all Northern Hemisphere stations show a breakpoint around 2014/2015. Prior to this breakpoint, the estimated slopes range from 0.8% to 8.8% per year, while after the breakpoint, they range from −0.4% to −2.2% per year. The confidence intervals indicate that most of these slopes are statistically significantly different from zero. More interestingly, for the majority of stations in the Northern Hemisphere, the intervals shift from positive to negative, suggesting a trend reversal from growth to decline. The three approaches applied in this paper should be seen as complementary rather than competing methods. Due to the characteristics of the data mentioned above, the extraction of trend reversals in the ethane burden can be a challenging task. By applying these methods in combination, they can provide stronger evidence of the presence of trend reversals in the data.

Overall, the consistency of our results across the different modeling approaches provides evidence that ethane levels in the Northern Hemisphere have been declining since 2015. In contrast, the Southern Hemisphere does not show a clear common trending pattern. While

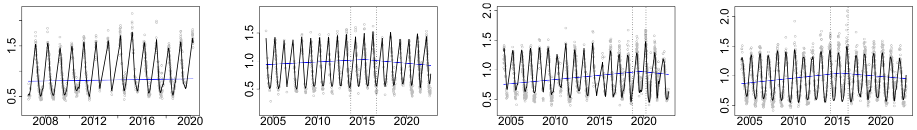

(a) Eureka (b) Ny-Alesund (c) Thule (d) Kiruna

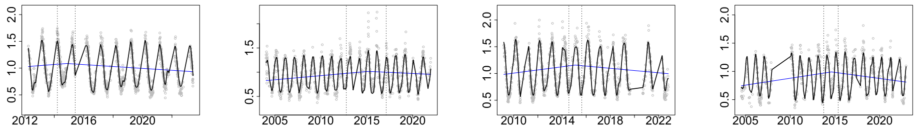

(e) Sodankyla (f) Harestua (g) St.Petersburg (h) Bremen

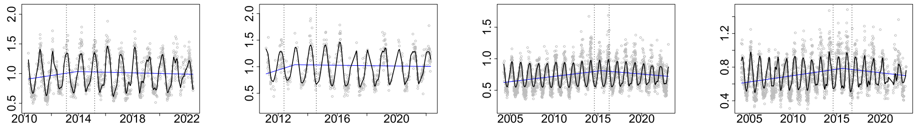

(i) Karlsruhe (j) Paris (k) Zugspitze (l) Jungfraujoch

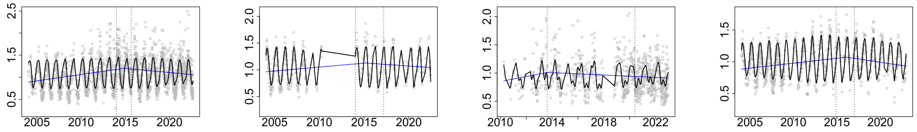

(m) Toronto (n) Rikubetsu (o) Boulder (p) Tsukuba

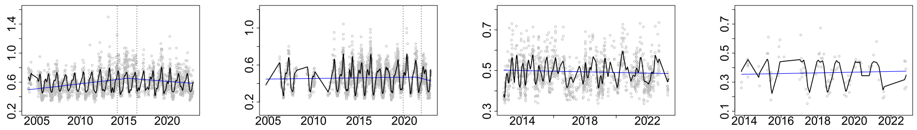

(q) Izana (r) Mauna Loa (s) Altzomoni (t) Paramaribo

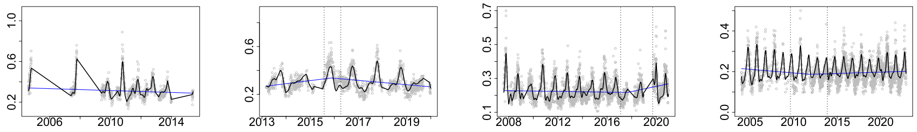

(u) REU - St.Denis (v) REU - Maido (w) Wollongong (x) Lauder

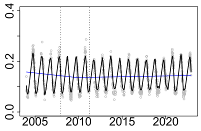

(y) Arrival Heights

Fig. 6 Results of the linear trend analysis as in Friedrich et al. (2020a). Dry-air mole fractions in ppb are given by the grey circles, the (broken) linear trend by the blue line, and the seasonal fit of the UCTSM by the black line. The dotted vertical lines (if present) are the confidence intervals around the break location this most recent trend reversal in the Northern Hemisphere has been attributed to a decline in oil prices, it remains an interesting topic for future research. It would imply that we should later see the impact of the war in Ukraine, resulting in a renewed interest and related boom in fracking in the U.S. and elsewhere to cover the European need for non-Russian gas and oil. In addition, future research could explore the commonalities in these trending behaviors through multivariate statistical analysis and consider additional factors causing the observed trends, such as shale gas production. The methods applied in this paper may also be used in a forecasting exercise to predict future ethane abundances.

Appendix A. Technical details

A.1. Nonparametric trend: a global smoothness parameter

To obtain a smoothness parameter that is optimal for multiple stations jointly, we first need to extend our nonparametric trend model to account for multiple time series:

$$y_{i,t} = \mu_{i,t} + \psi_{i,t} + \varepsilon_{i,t}, \qquad i = 1, \ldots, N, \quad t = 1, \ldots, T, \tag{A1}$$

where i is an index referring to station i with $i = 1, \ldots, N$. Similarly, $\psi_{i,t}$ represents the seasonal effects of the i_{th} station at time t. To study the long-run comovement, we now specify $\mu_{i,t}$ as follows:

$$\mu_{i,t} = d_i + g(t/T), \qquad i = 1, \ldots, N, \quad t = 1, \ldots, T, \tag{A2}$$

where d_i is a deterministic term that captures the level of ethane for each individual station. As in Sect. 4, the function $g(\cdot) : [0,1] \to \mathbb{R}$ denotes a smooth, nonrandom function that drives the variations of ethane globally. Hence, we drop the index i in $g(\cdot)$. To formally account for missing data, we define a sequence of binary variables $\{M_{i,t}\}$:

$$M_{i,t} = \begin{cases} 1, & \text{if } y_{i,t} \text{ is observed}, \\ 0, & \text{if } y_{i,t} \text{ is missing}, \end{cases} \qquad i = 1, \ldots, N, \quad t = 1 \ldots, T, \tag{A3}$$

where the missing data generating mechanism is assumed to satisfy the conditions mentioned in Friedrich et al. (2020b).

Given the specification (A2), it is straightforward to obtain a consistent estimator of $g(\cdot)$ by first partializing out the intercepts d_i and the seasonality component $\psi_{i,t}$ from $y_{i,t}$. As such, for each station i, we remove the seasonality of the ethane series using the Fourier terms in (A10), then centralize/demean the data. We then obtain a deseasonalized series $\{\tilde{y}_{i,t},\, t = 1, \ldots, T\}$ with zero average, i.e., $T^{-1} \sum_{t=1}^{T} M_{i,t} \tilde{y}_{i,t} = 0$, $i = 1, \ldots, N$.

We next consider the local linear estimation to estimate $g(\cdot)$. This nonparametric estimation method has been previously adopted for trending panel data models, for instance, see Li et al. (2011), Chen et al. (2012), Lin et al. (2023), and Friedrich et al. (2025). More specifically, let $g^{(1)}(\cdot)$ be the first order derivative of $g(\cdot)$. Moreover, we define $\tilde{\boldsymbol{y}}_i = (\tilde{y}_{i,1}, \ldots, \tilde{y}_{i,T})'$ and $\boldsymbol{Z}(\tau) = (\boldsymbol{z}_1, \ldots, \boldsymbol{z}_T)'$, where $\boldsymbol{z}_t(\tau) = (1, t/T - \tau)'$. For every fixed $\tau \in [0,1]$, then the local linear estimator of $g(\tau)$ is the first element in $\left(\hat{g}(\tau), \hat{g}^{(1)}(\tau)\right)'$, which is obtained by minimizing the following locally weighted sum of squares:

$$\begin{aligned}\begin{pmatrix}\hat{g}(\tau)\\ \hat{g}^{(1)}(\tau)\end{pmatrix} &= \text{argmin}_{(g(\tau),g^{(1)}(\tau))'} \sum_{i=1}^{N}\sum_{t=1}^{T} K\left(\frac{t/T-\tau}{h}\right) M_{i,t}\left[\tilde{y}_{i,t} - g(\tau) - g^{(1)}(\tau)\,(t/T-\tau)\right]^2 \\ &= \left[\sum_{i=1}^{N}\sum_{t=1}^{T} K\left(\frac{t/T-\tau}{h}\right) M_{i,t}\boldsymbol{z}_t(\tau)\boldsymbol{z}_t(\tau)'\right]^{-1}\left[\sum_{i=1}^{N}\sum_{t=1}^{T} K\left(\frac{t/T-\tau}{h}\right) M_{i,t}\boldsymbol{z}_t(\tau)\tilde{y}_{i,t}\right] \\ &= \left[\sum_{i=1}^{N}\boldsymbol{Z}(\tau)'\boldsymbol{W}_i(\tau,h)\boldsymbol{Z}(\tau)\right]^{-1}\sum_{i=1}^{N}\boldsymbol{Z}(\tau)'\boldsymbol{W}_i(\tau,h)\tilde{\boldsymbol{y}}_i,\end{aligned} \tag{A4}$$

where $K(\cdot)$ is a kernel function, $h > 0$ is a use-specified bandwidth parameter, and

$$\boldsymbol{W}_i(\tau,h) = \text{diag}\left\{K\left(\frac{1/T-\tau}{T}\right)M_{i,1},\ldots,K\left(\frac{T/T-\tau}{T}\right)M_{i,T}\right\}, \qquad i=1,\ldots,N, \tag{A5}$$

are T-dimensional diagonal weighting matrices. The selection of $K(\cdot)$ usually does not lead to a qualitative difference. We use the Epanechnikov kernel $K(x) = 3/4(1-x^2)\mathbb{1}_{\{|x|\leq 1\}}$ in our analysis. The bandwidth parameter h, which is *common* for all i, controls the level of overall smoothness. As discussed in Sect. 4, a data-driven method can assist the selection in practice. We consider the Modified Cross-Validation (MCV) loss criterion:

$$\text{MCV}(h) = (NT)^{-1}\sum_{i=1}^{N}\sum_{t=1}^{T}\left[\tilde{y}_{i,t} - \hat{g}_{l,h}(t/T)\right]^2, \tag{A6}$$

where $\hat{g}_{l,h}(t/T)$ is the leave-$(2l+1)$-out estimator obtained by omitting observations at $t = \lfloor \tau T \rfloor + i$, $-l \leq i \leq l$, $\tau \in [0,1]$. We have that $\left(\hat{g}_{l,h}(\tau), \hat{g}^{(1)}_{l,h}(\tau)\right)'$ equals

$$\left[\sum_{i=1}^{N}\sum_{t:|t-\tau T|>l} K\left(\frac{t/T-\tau}{h}\right) M_{i,t}\boldsymbol{z}_t\boldsymbol{z}_t'\right]^{-1}\left[\sum_{i=1}^{N}\sum_{t:|t-\tau T|>l} K\left(\frac{t/T-\tau}{h}\right) M_{i,t}\boldsymbol{z}_t\tilde{y}_{i,t}\right].$$

Conventionally, the optimal bandwidth $\hat{h}_{\text{opt}}$ is the minimizer of the MCV criterion:

$$\hat{h}_{\text{opt}} = \underset{h\in\mathbb{H}}{\text{argmin}}\,\text{MCV}(h), \qquad \mathbb{H} \subset \mathbb{R}. \tag{A7}$$

Therefore, the method is fully data-driven whenever the value of l and the parameter space $\mathbb{H}$ are specified.

We make the following remarks. Firstly, the leave-$(2l+1)$-out estimator above only removes observations along the time dimension. Indeed, if N is sufficiently large, one may also implement the leave-one-unit-out cross-validation method by removing observations along the cross-sectional dimension as in Chen et al. (2012).

More importantly, the minimization step (A7) can be problematic, especially when constructing simultaneous confidence bands as discussed, for instance, in Friedrich and Lin (2024) and Lin et al. (2025). The issue mostly stems from the choice of $\mathbb{H}$, more specifically here, the upper bound of $\mathbb{H}$. For illustration, we take $l=0$ and $\mathbb{H} = \{0.05, 0.055, \ldots, 0.245, 0.25\}$, yielding a grid of 41 points. For the global trend estimations, different values of l do not lead to a significant difference; the results are thus omitted. The MCV criteria using the data of the Northern and Southern Hemispheres are plotted in Fig. A1 separately. We observe that the loss function for the Northern Hemisphere monotonically decreases when $h \in \mathbb{H}$ is large enough. As such, the minimization rule (A7) often selects the upper bound of $\mathbb{H}$, making the results sensitive to the choice of $\mathbb{H}$. The figure also demonstrates that the MCV, or many other common data-driven methods, can have multiple local minima. For estimating $g(\cdot)$, we prefer a small bandwidth that can capture important, local movements in the trend curves while still producing a reasonably smooth estimate. Here we find that the second smallest local minimum for the Northern Hemisphere leads to satisfactory results, and the third one for the southern stations. Namely, we shall take the values of 0.09 and 0.125 for the Northern and Southern Hemispheres, respectively.

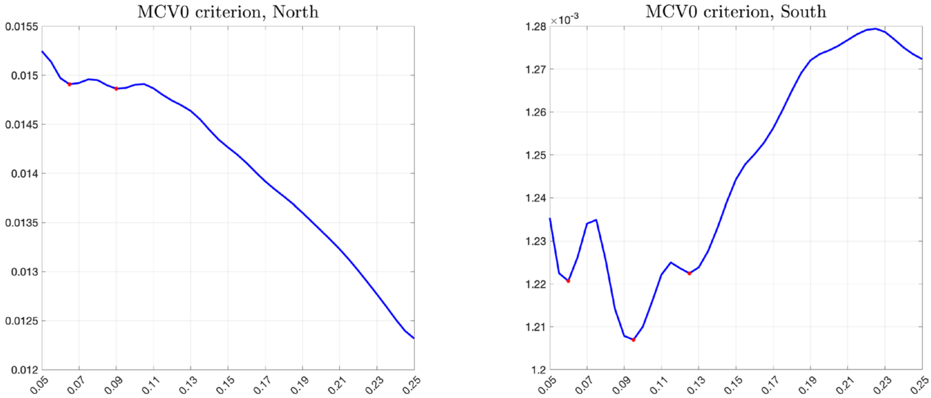

Fig. A1 Modified Cross-Validation (MCV) criterion over an equidistant grid of 41 points in $[0.05, 0.25]$ with a mesh of 0.005, based on the leave-$(2l+1)$-out estimator with $l=0$. For the stations in the Northern Hemisphere (left), the two local minima are located at 0.065, and 0.09. For the stations in the Southern Hemisphere (right), the three local minima are located at 0.06, 0.095 and 0.125

A.2. Unobserved components time series model

The unobserved components time series model (UCTSM) is considered for the seasonal adjustment of the ethane tine series from all stations, see Sect. 2, and for the trend estimation in Sect. 5. The UCTSM is developed and explored in detail by Harvey (1989). It has a measurement equation that is the same as Eq. (1) and is given by

$$y_t = \mu_t + \psi_t + \varepsilon_t, \qquad \varepsilon_t \overset{\text{i.i.d.}}{\sim} \mathcal{N}(0, \sigma_\varepsilon^2), \tag{A8}$$

but we assume that the stochastic disturbance variable ε_t is independently and identically distributed (i.i.d.), and has a Gaussian density with mean zero and variance $\sigma_\varepsilon^2 > 0$, that is $\mathcal{N}(0, \sigma_\varepsilon^2)$. The trend μ_t and seasonal ψ_t components are formulated as dynamic stochastic processes. The trend component μ_t is specified as an integrated random walk process given by

$$\mu_{t+1} = \mu_t + \beta_t, \qquad \beta_{t+1} = \beta_t + \zeta_t, \quad \zeta_t \overset{\text{i.i.d.}}{\sim} \mathcal{N}(0, \sigma_\zeta^2), \tag{A9}$$

where β_t is the growth, gradient or slope of μ_t and ζ_t is the innovation or disturbance driving the time-varying trend component. The disturbances ε_t in Eq. (A8) and ζ_t in Eq. (A9) are assumed to be mutually and serially independent of each other. The role of μ_t is to account for the low-frequency year-on-year dynamics in the time series y_t. The seasonal within-year component ψ_t is modeled as a sum of three dynamic stochastic processes specified as time-varying Fourier series with different seasonal frequencies. In particular, we have

$$\psi_t = \sum_{s=1}^{S} \psi_t^{(s)}, \tag{A10}$$

where each individual Fourier process $\psi_t^{(s)}$ is specified as

$$\begin{pmatrix} \psi_{t+1}^{(s)} \\ \psi_{t+1}^{(s)*} \end{pmatrix} = \begin{bmatrix} \cos\lambda_s & \sin\lambda_s \\ -\sin\lambda_s & \cos\lambda_s \end{bmatrix} \begin{pmatrix} \psi_t^{(s)} \\ \psi_t^{(s)*} \end{pmatrix} + \begin{pmatrix} \omega_t^{(s)} \\ \omega_t^{(s)*} \end{pmatrix}, \tag{A11}$$

and

$$\lambda_s = \frac{2\pi\, s}{365.25}, \qquad \omega_t^{(s)}, \omega_t^{(s)*} \overset{\text{i.i.d.}}{\sim} \mathcal{N}(0, \sigma_\omega^2), \qquad s = 1, \ldots, S.$$

The disturbances ε_t in Eq. (A8), ζ_t in Eq. (A9) and $\omega_t^{(s)}$ and $\omega_t^{(s)*}$ in Eq. (A11) are assumed to be mutually and serially independent of each other, at all time points, and for all $s = 1, \ldots, S$. All seasonal disturbances are assumed to share the same variance σ_ω^2 to keep the number of unknown parameters to a minimum. The dynamic specification for $\psi_t^{(s)}$ in Eq. (A11) relies fully on the auxiliary variable $\psi_t^{(s)*}$ that plays a similar role to β_t in Eq. (A9). The choice of the number of time-varying Fourier terms, S, can be based on formal statistical procedures such as the likelihood ratio (LR) test or the well-known Akaike information criterion (AIC). The specification of the UCTSM is completed with appropriate initial conditions for the unobserved components and their auxiliary variables β_t and $\psi_t^{(s)*}$. We refer to the discussion in Durbin and Koopman (2012, Ch. 5) on initialization issues for the recursions in Eqs. (A9) and (A11). Alternative specifications for the seasonal component in a UCTSM are discussed by Proietti (2000).

The UCTSM can be formulated as a linear Gaussian state space model consisting of an observation equation for y_t and an update equation for the state vector α_t comprising all unobserved components together with their auxiliary variables. For our model with S=3, we have

$$\boldsymbol{\alpha}_t = \left(\mu_t\,,\, \beta_t\,,\, \psi_t^{(1)}\,,\, \psi_t^{(1)*}\,,\, \psi_t^{(2)}\,,\, \psi_t^{(2)*}\,,\, \psi_t^{(3)}\,,\, \psi_t^{(3)*}\right)'.$$

The state space model has the general observation equation $y_t = \boldsymbol{Z}\boldsymbol{\alpha}_t + \varepsilon_t$, with the selection matrix $\boldsymbol{Z}$ which for the UCTSM (A8) is given by $\boldsymbol{Z} = (1, 0, 1, 0, 1, 0, 1, 0)$, and the state updating equation $\boldsymbol{\alpha}_{t+1} = \boldsymbol{T}\boldsymbol{\alpha}_t + \boldsymbol{\eta}_t$, with, following from Eqs. (A9) and (A11), the transition matrix $\boldsymbol{T}$ as given by

$$\boldsymbol{T} = \begin{bmatrix} 1 & 1 & 0 & 0 & 0 & 0 & 0 & 0 \\ 0 & 1 & 0 & 0 & 0 & 0 & 0 & 0 \\ 0 & 0 & \cos\lambda_1 & \sin\lambda_1 & 0 & 0 & 0 & 0 \\ 0 & 0 & -\sin\lambda_1 & \cos\lambda_1 & 0 & 0 & 0 & 0 \\ 0 & 0 & 0 & 0 & \cos\lambda_2 & \sin\lambda_2 & 0 & 0 \\ 0 & 0 & 0 & 0 & -\sin\lambda_2 & \cos\lambda_2 & 0 & 0 \\ 0 & 0 & 0 & 0 & 0 & 0 & \cos\lambda_3 & \sin\lambda_3 \\ 0 & 0 & 0 & 0 & 0 & 0 & -\sin\lambda_3 & \cos\lambda_3 \end{bmatrix}$$

and with the state disturbance vector $\boldsymbol{\eta}_t = (0, \zeta_t, \omega_t^{(1)}, \omega_t^{(1)*}, \omega_t^{(2)}, \omega_t^{(2)*}, \omega_t^{(3)}, \omega_t^{(3)*})'$. The variance matrix of the state disturbance vector is given by

$$\boldsymbol{\Sigma}_\eta = \begin{bmatrix} 0 & 0 & 0 \\ 0 & \sigma_\zeta^2 & 0 \\ 0 & 0 & \sigma_\omega^2 \boldsymbol{I}_6 \end{bmatrix},$$

where $\boldsymbol{I}_p$ is the $p \times p$ identity matrix. These system matrices $\boldsymbol{Z}$, $\boldsymbol{T}$, $\boldsymbol{\Sigma}_\eta$ and σ_ε^2 determine the dynamic and statistical properties for y_t as implied by the UCTSM. Furthermore, the system matrices can partly depend on a set of unknown parameters, which for this UCTSM are only in σ_ε^2 and $\boldsymbol{\Sigma}_\eta$. We collect the unknown variances in the parameter vector $\boldsymbol{\phi} = (\sigma_\varepsilon^2, \sigma_\zeta^2, \sigma_\omega^2)'$.

Once the model is represented in state space form, the Kalman filter and related state space methods can be applied. The initialization of the Kalman filter recursions is based on the assumption of having a diffuse prior for $\boldsymbol{\alpha}_1$. A particularly convenient feature of state space methods is that they can handle missing observations in a statistically correct manner. We estimate the unknown parameters in $\boldsymbol{\phi}$ by the method of maximum likelihood; the numerical maximization of the likelihood function with respect to the parameter vector $\boldsymbol{\phi}$ requires the Kalman filter to compute the log likelihood function repeatedly during the maximization process. Once the estimate of ϕ is obtained, we can compute the standardized prediction errors from the Kalman filter and use these for diagnostic checking and model evaluations. For both seasonal adjustment and trend extraction, We require the smoothed estimates of the unobserved trend μ_t and the periodic within-year component ψ_t, these are estimates based on all observations. We can obtain them from a Kalman filter (forward step) and a related smoothing method (backward step). More specific details of the state space formulation and the state space methods are discussed in Durbin and Koopman (2012).

Appendix B. Further analysis of the trend models

In this section, we present additional results. Figure B1 presents the yearly mean trend estimates from both the nonparametric and state-space approaches. To highlight the trend reversal around 2014/2015, we focus on the period 2010–2020. The outcome of the break tests that aided the results in Sect. 6 are given in Table B1. It shows the sample period, the number of observations T together with the p-value, the test statistic (F_T), and the AWB

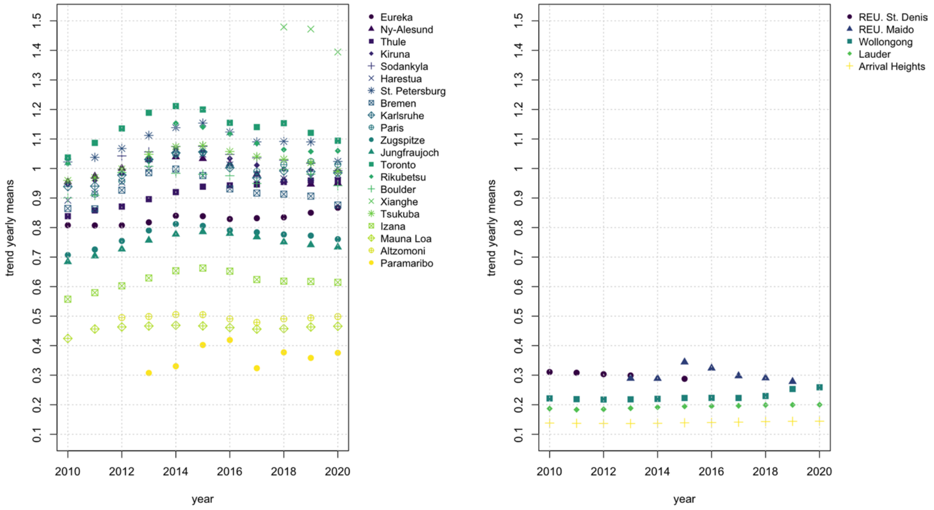

(a) Northern Hemisphere, Nonparametric (b) Southern Hemisphere, Nonparametric

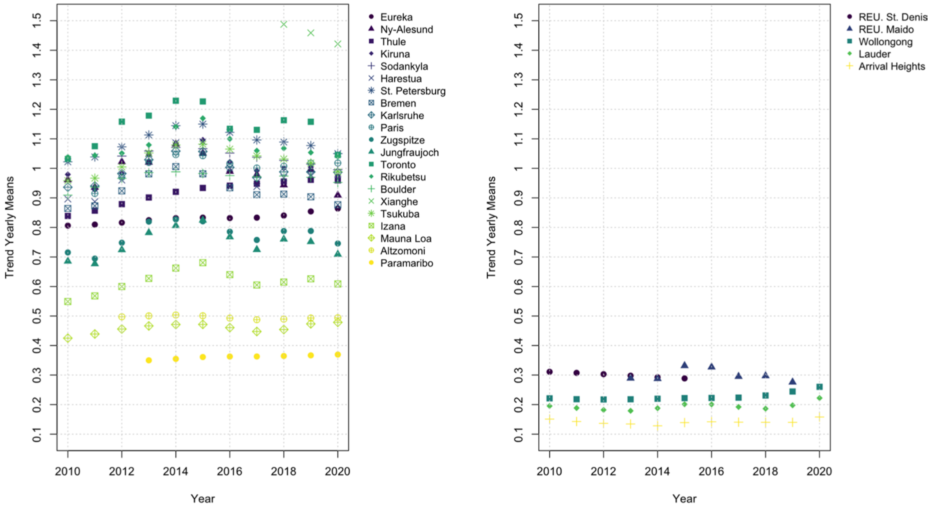

(c) Northern Hemisphere, UCTSM (d) Southern Hemisphere, UCTSM

Fig. B1 Yearly mean trend estimates (2010–2020) obtained from the nonparametric method in Sect. 4 and from the UCTSM approach in Sect. 5. Stations are sorted according to decreasing latitude for the Northern Hemisphere and increasing latitude for the Southern Hemisphere

critical value associated with the break test at a significance level of 5%. Low (high) values of F_T indicate little (substantial) evidence in favor of the model with a structural break. We can see that the test detects a break in all time series with the exception of Eureka, Altzomoni, Paramaribo, and St. Denis.

Additionally, we investigate the residuals obtained from our models using a Ljung-Box test. In Table B2, the results of Ljung-Box tests for residual autocorrelation, including up to 20 lags, are given. The columns present the test statistics applied to residuals from the nonparametric trend model of Sect. 4, the UCTSM model of Sect. 5, and the (broken) lin-

Table B1 Results from the bootstrapped break test of Friedrich et al. (2020a) (with $\lambda = 0.1$), sorted according to latitude

Station	Period	T	*p*-value	S_T	critical value
Northern Hemisphere					
Eureka	2006–2020	828	0.229	0.035	0.072
Ny-Ålesund	1993–2022	882	0.000	0.654	0.124
Thule	1999–2021	1,464	0.000	0.518	0.096
Kiruna	1996–2022	1,924	0.000	1.779	0.191
Harestua	1994–2021	1,224	0.000	0.670	0.178
St. Petersburg	2009–2022	906	0.000	2.150	0.167
Bremen	2004–2022	544	0.000	2.086	0.154
Karlsruhe	2010–2022	1,162	0.000	0.843	0.115
Paris	2011–2022	551	0.002	0.498	0.185
Zugspitze	1995–2020	2,237	0.000	2.834	0.215
Jungfraujoch	1986–2022	3,171	0.000	5.662	0.296
Toronto	2002–2022	2,377	0.000	9.039	0.865
Rikubetsu	1995–2022	1,078	0.000	0.451	0.102
Boulder	2010–2021	788	0.030	0.396	0.339
Xianghe	2018–2021	706			
Tsukuba	2001–2022	1,089	0.000	1.539	0.121
Izaña	1999–2021	2,244	0.000	1.792	0.170
Mauna Loa	1995–2021	2,746	0.000	0.135	0.041
Altzomoni	2012–2022	1,140	0.683	0.007	0.038
Paramaribo	2013–2022	102	0.126	0.026	0.037
Southern Hemisphere					
La Réunion, St. Denis	2004–2015	745	0.383	0.042	0.121
La Réunion, Maïdo	2013–2019	1,095	0.000	0.448	0.037
Wollongong	2007–2020	2,324	0.000	0.267	0.036
Lauder	1996–2022	3,426	0.000	0.089	0.014
Arrival Heights	1997–2022	1,130	0.000	0.017	0.002

ear trend model of Sect. 6. Given the high values of the test statistics, the results indicate that there is remaining autocorrelation present in the residuals of most models. This further underlines the need to apply robust inference methods, such as the autoregressive wild bootstrap, which is employed in Sects. 4 and 6. For the UCTSM model, we further analyze how strong the remaining autocorrelation is with the help of the autocorrelation functions (ACF) of the residuals. In Fig. B2, we plot the ACF values for up to 20 lags. For most stations, the ACFs show some significant spikes at one lag, but the autocorrelation rarely exceeds values of 0.2. Exceptions to this are seen at Mauna Loa, Altzomoni, La Réunion and Wollongong.

Finally, we perform a bivariate correlation analysis between the (monthly averaged) estimated trends from the UCTSM model and a set of potential explanatory variables. Those are the monthly U.S. production of crude oil, U.S. gross withdrawals of natural gas, and U.S. gross withdrawals of shale gas, obtained from the U.S. Energy Information Administration

Table B2 Test statistics from Ljung-Box tests for residual autocorrelation on the residuals of each model. The test is performed with 20 lags

Station	Nonpara. trend	UCTSM	Lin. trend
Northern Hemisphere			
Eureka	112.00	121.10	114.75
Ny-Ålesund	383.04	62.42	322.82
Thule	172.26	200.67	193.93
Kiruna	513.53	153.61	443.16
Harestua	113.26	73.40	324.32
St. Petersburg	118.98	91.18	106.99
Bremen	35.34	55.54	52.25
Karlsruhe	94.95	72.46	100.41
Paris	54.32	47.27	48.42
Zugspitze	161.00	100.48	194.97
Jungfraujoch	349.95	168.00	225.86
Toronto	90.39	67.14	123.99
Rikubetsu	266.87	29.22	45.12
Boulder	33.17	35.78	29.98
Xianghe	33.73	22.51	–
Tsukuba	23.63	23.62	50.31
Izaña	189.69	214.45	198.15
Mauna Loa	813.53	863.88	671.88
Altzomoni	242.34	226.46	217.87
Paramaribo	18.45	37.62	35.31
Southern Hemisphere			
La Réunion, St. Denis	590.20	248.19	217.03
La Réunion, Maïdo	232.58	229.07	528.30
Wollongong	2398.09	381.49	425.80
Lauder	1726.82	219.80	1142.64
Arrival Heights	1254.57	42.81	920.62

(https://www.eia.gov). The results are presented in Table B3. The columns give the pairwise Pearson correlation coefficient for crude oil production, natural gas, and shale gas withdrawals, respectively. Although this analysis should be seen as a descriptive rather than a formal statistical analysis, it can shed some light on the relation between ethane trends, and oil and gas production. Most estimated trends from the Northern Hemisphere show a positive correlation with the explanatory variables. Exceptions are Ny-Ålesund, St. Petersburg, Bremen, Jungfraujoch, Boulder, Xianghe, and Altzomoni, where some of the coefficients are negative. In the Southern Hemisphere, the estimated trends mostly exhibit a negative correlation with the oil, gas, and shale gas variables (with the exception of Wollongong). The average correlations between all three variables and the estimated trends are positive in the Northern Hemisphere and negative in the Southern Hemisphere. These results are mostly in line with Maddanu and Proietti (2023) who perform a regression analysis of the estimated trends on U.S. crude oil production and U.S. natural gas gross withdrawals.

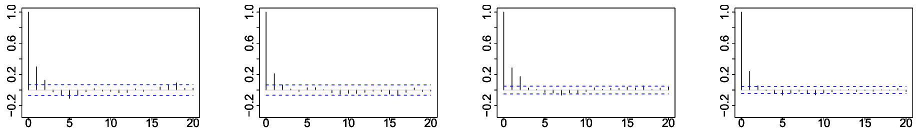

(a) Eureka (b) Ny-Alesund (c) Thule (d) Kiruna

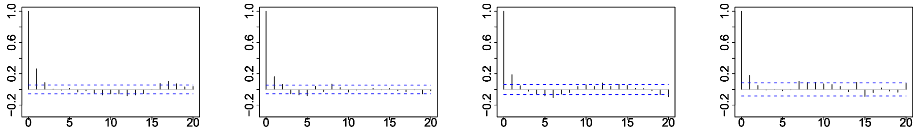

(e) Sodankyla (f) Harestua (g) St. Petersburg (h) Bremen

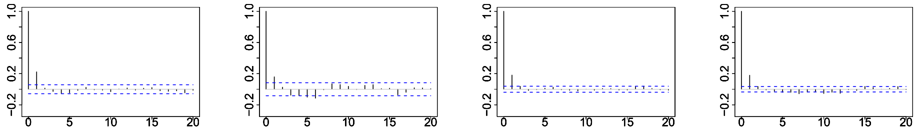

(i) Karlsruhe (j) Paris (k) Zugspitze (l) Jungfraujoch

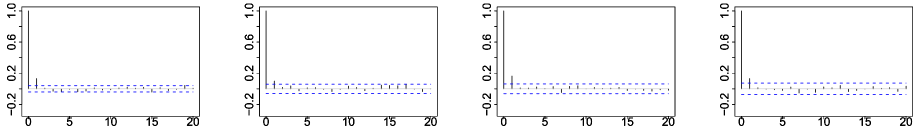

(m) Toronto (n) Rikubetsu (o) Boulder (p) Xianghe

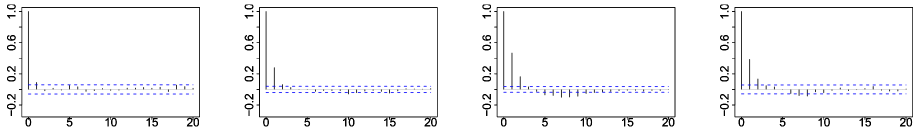

(q) Tsukuba (r) Izana (s) Mauna Loa (t) Altzomoni

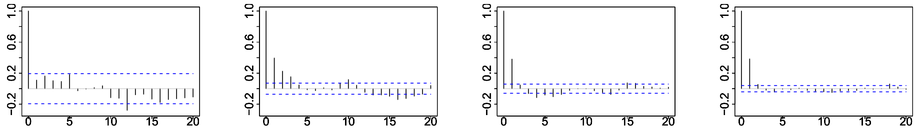

(u) Paramaribo (v) REU - St. Denis (w) REU - Maido (x) Wollongong

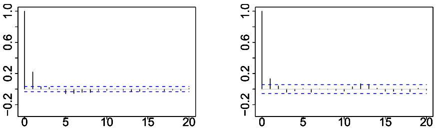

(y) Lauder (z) Arrival Heights

Fig. B2 Plots of the correlation between the residuals from the UCTSM and their respective lags, plotted as a function of up to 20 lags. The dashed horizontal lines give an approximate 95% confidence interval at $-\frac{1.95}{\sqrt{T}}$ and $\frac{1.95}{\sqrt{T}}$

Table B3 Correlation analysis between the monthly averaged estimated UCTSM trends per station and time series of U.S. crude oil production, U.S. natural gas gross withdrawals and U.S. shale gas withdrawals. The values indicate the pairwise Pearson correlation coefficient

Station	Crude oil	Natural gas	Shale gas
Northern Hemisphere			
Eureka	0.976	0.933	0.957
Ny-Ålesund	−0.176	−0.348	−0.07
Thule	0.856	0.874	0.897
Kiruna	0.506	0.421	0.324
Harestua	0.606	0.483	0.507
St. Petersburg	0.101	−0.153	−0.093
Bremen	0.292	0.199	−0.088
Karlsruhe	0.355	0.216	0.217
Paris	0.534	0.296	0.337
Zugspitze	0.551	0.423	0.362
Jungfraujoch	0.423	−0.139	0.360
Toronto	0.591	0.501	0.398
Rikubetsu	0.389	0.273	0.398
Boulder	−0.023	−0.291	−0.240
Xianghe	0.243	−0.490	−0.805
Tsukuba	0.496	0.346	0.174
Izaña	0.704	0.622	0.469
Mauna Loa	0.162	−0.027	0.559
Altzomoni	−0.588	−0.659	−0.745
Paramaribo	0.755	0.881	0.931
Average North	**0.360**	**0.218**	**0.223**
Southern Hemisphere			
La Réunion, St. Denis	−0.823	−0.933	−0.977
La Réunion, Maïdo	−0.243	−0.249	−0.261
Wollongong	0.455	0.557	0.492
Lauder	−0.215	−0.353	0.111
Arrival Heights	−0.275	−0.390	0.040
Average South	**−0.220**	**−0.274**	**−0.119**

Acknowledgements We thank Bernhard van der Sluis for his excellent research assistance. The Eureka measurements were made at the Polar Environment Atmospheric Research Laboratory (PEARL), and the Toronto measurements were made at the University of Toronto Atmospheric Observatory (TAO); both are primarily supported by the Natural Sciences and Engineering Research Council of Canada, the Canadian Space Agency, and Environment and Climate Change Canada. The Rikubetsu site is funded by the joint research program of the Institute for Space-Earth Environmental Research, Nagoya University. FTIR observations at the Rikubetsu and Tsukuba sites are supported in part by the GOSAT series project. Wolfgang Stremme and Alejandro Bezanilla are acknowledged for their contribution in the operation and data analysis of the Altzomoni station. Financial and technical support has been provided by ICAyCC and RUOA personnel from UNAM and through the DGAPA-PAPIIT IG101225 & IN106024 grants. Measurements made at Lauder and Arrival Heights are supported by NIWA through New Zealand's Ministry of Business, Innovation and Employment Strategic Science Investment Fund. We thank Antarctica New Zealand for logistical support. FTIR observations at St.Petersburg site were supported by Saint Petersburg State University, Project No. 132392751. The Paris site has received funding from Sorbonne Université, the French research center CNRS, and the French space agency CNES. Harestua FTIR measurements are supported by the Swedish Environmental Protection Agency. Funding via the Helmholtz ATMO programme has enabled the sustained NDACC FTIR activities at Izana since the late 1990s. In addition, the Izana NDACC FTIR observations strongly rely on the support (facilities and operational activities) of the Izana Atmospheric Research Centre of the Spanish Weather Service (AEMET), with lead contributions of O. E. García. Matthias Schneider and O. E. García are acknowledged for setting up the NDACC FTIR Izana site and performing the measurements. Thomas Blumenstock is acknowledged for setting up the NDACC FTIR Kiruna site and performing measurements. Uwe Raffalski is acknowledged for technical support and helping with measurements. The Xianghe FTIR measurements are supported by the National Key R&D Program (2023YFC3705202). This material is based upon work supported by the National Center for Atmospheric Research (NCAR), which is a major facility sponsored by the National Science Foundation under Cooperative Agreement No. 1852977. The NCAR FTS observation programs at Thule, GR, Boulder, CO, and Mauna Loa, HI are supported under contract by the National Aeronautics and Space Administration (NASA). This study has been supported under contract by the National Aeronautics and Space Administration (NASA) award No. NNX17AE38G. The Thule work is also supported by the NSF Office of Polar Programs (OPP). We wish to thank the Danish Meteorological Institute for support at the Thule site and NOAA for support of the MLO site. The Wollongong data is supported by work undertaken through Australian Research Council grants. We thank the FTIR-Team at IMK-IFU, Garmisch for providing ethane data retrieved from FTIR solar absorption measurements at the Zugspitze station, Germany. The ULiège contribution to this work was primarily supported by the Fonds de la Recherche Scientifique (F.R.S. - FNRS, Brussels, Belgium) and the GAW-CH program of MeteoSwiss (Zürich, CH). EM is a Research Director with F.R.S. - FNRS. The ULiège team thanks the International Foundation High Altitude Research Stations Jungfraujoch and Gornergrat (HFSJG, Bern, CH) for supporting the facilities needed to perform the Fourier Transform InfraRed observations at Jungfraujoch. Marina Friedrich acknowledges funding from the Nederlandse Organisatie voor Wetenschappelijk Onderzoek (NWO) as part of project VI.Veni0.231E0.033.

Author contribution Marina Friedrich, Siem Jan Koopman, Yicong Lin, Emmanuel Mahieu, Stephan Smeekes: Conceptualization, Data curation, Funding acquisition, Investigation, Methodology, Project administration, Supervision, Writing - original draft, review & editing. Martine De Mazière, Victoria Flood, Matthias Max Frey, Michel Grutter, James W. Hannigan, Frank Hase, Nicholas Jones, Rigel Kivi, Maria Makarova, Isamu Morino, Isao Murata, Tomoo Nagahama, Justus Notholt, Ivan Ortega, Maxime Prignon, Amelie Ninja Röhling, Dan Smale, Kimberly Strong, Yao Té, Minqiang Zhou: Data curation, Writing - review & editing.

Data availability The data used in this publication were obtained from the Network for the Detection of Atmospheric Composition Change (NDACC) and are available through the NDACC website http://www.ndacc.org. They can additionally be made available from the authors upon reasonable request.

Declarations

Competing interests The authors have no relevant financial or non-financial interests to disclose.

References

Angelbratt J, Mellqvist J, Simpson D, Jonson JE, Blumenstock T, Borsdorff T, Duchatelet P, Forster F, Hase F, Mahieu E, De Mazière M, Notholt J, Petersen AK, Raffalski U, Servais C, Sussmann R, Warneke T, Vigouroux C (2011) Carbon monoxide (co) and ethane (c_2h_6) trends from ground-based solar FTIR measurements at six European stations, comparison and sensitivity analysis with the EMEP model. Atmos Chem Phys 11(17):9253–9269

Angot H, Davel C, Wiedinmyer C, Pétron G, Chopra J, Hueber J, Blanchard B, Bourgeois I, Vimont I, Montzka SA, Miller BR, Elkins JW, and Helmig D (2021) Temporary pause in the growth of atmospheric ethane and propane in 2015–2018. Atmos Chem Phys 21(19):15153–15170

Batchelor RL, Strong K, Lindenmaier R, Mittermeier RL, Fast H, Drummond JR, Fogal PF (2009) A new bruker IFS 125hr FTIR spectrometer for the polar environment atmospheric research laboratory at Eureka, Nunavut, Canada: measurements and comparison with the existing Bomem DA8 spectrometer. J Atmos Ocean Technol 26(7):1328–1340

Baylon JL, Stremme W, Grutter M, Hase F, Blumenstock T (2017) Background CO_2 levels and error analysis from ground-based solar absorption IR measurements in central Mexico. Atmos Meas Techniques 10(7):2425–2434

Beutner E, Lin Y, Smeekes S (2023) GLS estimation and confidence sets for the date of a single break in models with trends. Econometric Rev 42(2):195–219

Blumenstock T, Hase F, Kramer I, Mikuteit S, Fischer H, Goutail F, Raffalski U (2009) Winter to winter variability of chlorine activation and ozone loss as observed by ground-based FTIR measurements at Kiruna since winter 1993/94. Int J Remote Sens 30(15–16):4055–4064

Cai Z (2007) Trending time-varying coefficient time series models with serially correlated errors. J Econom 136:163–188

Chen J, Gao J, Li D (2012) Semiparametric trending panel data models with cross-sectional dependence. J Econom 171(1):71–85

Chu C-K, Marron JS (1991) Comparison of two bandwidths selectors with dependent errors. Ann Stat 19(4):1906–1918

Durbin J, Koopman SJ (2012) Time series analysis by state space methods. 2nd edn. Oxford University Press, Oxford

Franco B, Bader W, Toon GC, Bray C, Perrin A, Fischer EV, Sudo K, Boone CD, Bovya B, Lejeune B, Servais C, Mahieu E (2015) Retrieval of ethane from ground-based FTIR solar spectra using improved spectroscopy: recent burden increase above Jungfraujoch. J Quant Spectrosc Radiat Transf 160:36–49

Franco B, Mahieu E, Emmons LK, Tzompa-Sosa ZA, Fischer EV, Sudo K, Bovy B, Conway S, Griffin D, Hannigan JW, Strong K, Walker KA (2016) Evaluating ethane and methane emissions associated with the development of oil and natural gas extraction in North America. Environ Res Lett 11(4):44010

Friedrich M, Beutner E, Reuvers H, Smeekes S, Urbain J-P, Bader W, Franco B, Lejeune B, Mahieu E (2020a) A statistical analysis of time trends in atmospheric ethane. Climatic Change 162:105–125

Friedrich M, Lin Y (2024) Sieve bootstrap inference for linear time-varying coefficient models. J Econom 239(1):105345

Friedrich M, Lin Y, Ramdaras P, Telg S, van der Sluis B (2025) Modelling time-varying relations in housing prices: a semiparametric panel approach. J R Stat Soc Ser C Appl Stat:qlaf020

Friedrich M, Smeekes S, Urbain J (2020b) Autoregressive wild bootstrap inference for nonparametric trends. J Econom 214:81–109

García OE, Schneider M, Sepúlveda E, Hase F, Blumenstock T, Cuevas E, Ramos R, Gross J, Barthlott S, Röhling AN, Sanromá E, González Y, Gómez-Peláez AJ, Navarro-Comas M, Puentedura O, Yela M, Redondas A, Carreno V, León-Luis SF, Reyes E, García RD, Rivas PP, Romero-Campos PM, Torres C, Prats N, Hernández M, López C (2021) Twenty years of ground-based NDACC FTIR spectrometry at Iza na observatory – overview and long-term comparison to other techniques. Atmos Chem Phys 21(20):15519–15554

Griffith DWT, Deutscher NM, Velazco V, Jones NB, Paton Walsh C, Wilson SR (2021) TCCON and NDACC: 20 years of ground-based remote sensing of atmospheric trace gases at Wollongong and Darwin. Baseline Atmos Program Aust 2011–2013 csiro:EP2021-3762:55

Hannigan JW, Coffey MT, Goldman A (2009) Semiautonomous FTS observation system for remote sensing of stratospheric and tropospheric gases. J Atmos Ocean Technol 26(9):1814–1828

Harvey A, Koopman S, Riani M (1997) The modelling and seasonal adjustment of weekly observations. J Bus Econ Stat 15:354–368

Harvey AC (1989) Forecasting, structural time series models and the Kalman filter. 1st edn. Cambridge University Press

Harvey DI, Leybourne SJ (2014) Break date estimation for models with deterministic structural change. Oxford Bull Econ Stat 76:623–642

Hausmann P, Sussmann R, Smale D (2016) Contribution of oil and natural gas production to renewed increase in atmospheric methane (2007-2014): top-down estimate from ethane and methane column observations. Atmos Chem Phys 16(5):3227–3244

Kiel M, Hase F, Blumenstock T, Kirner O (2016) Comparison of XCO abundances from the total carbon column observing network and the network for the detection of atmospheric composition change measured in Karlsruhe. Atmos Meas Techniques 9(5):2223–2239

Kivi R, Heikkinen P (2016) Fourier transform spectrometer measurements of column CO_2 at Sodankylä, Finland. Geoscientific Instrum Methods Data Syst 5(2):271–279

Li D, Chen J, Gao J (2011) Non-parametric time-varying coefficient panel data models with fixed effects. Econom J 14(3):387–408

Lin Y, Song M, van der Sluis B (2025) Bootstrap inference for linear time-varying coefficient models in locally stationary time series. J Comput Graphical Stat 34(2):654–667

Lin Y, van der Sluis B, Friedrich M (2023) Bootstrapping trending time-varying coefficient panel models with missing observations. Tinbergen Institute Discussion Paper, 2023-079/III

Lutsch E, Strong K, Jones D, Blumenstock T, Conway S, Fisher J, Hannigan J, Hase F, Kasai Y, Mahieu E, Makarova M, Morino I, Nagahama T, Notholt J, Ortega I, Palm M, Poberovskii A, Sussmann R, Warneke T (2020) Detection and attribution of wildfire pollution in the Arctic and northern midlatitudes using a network of Fourier-transform infrared spectrometers and GEOS-Chem. Atmos Chem Phys 20(20):12813–12851

Maddanu F, Proietti T (2023) Trends in atmospheric ethane. Climatic Change 176(5):1–23

Makarova M, Poberovskii A, Polyakov A, Imkhasin KH, Ionov D, Makarov B, Kostsov V, Foka S, Abakumov E (2024) Trends of key greenhouse gases as measured in 2009–2022 at the FTIR station of St. Petersburg State University. Remote Sens 16(11)

Ortega I, Buchholz RR, Hall EG, Hurst DF, Jordan AF, Hannigan JW (2019) Tropospheric water vapor profiles obtained with FTIR: comparison with balloon-borne frost point hygrometers and influence on trace gas retrievals. Atmos Meas Techniques 12(2):873–890

Pardo Cantos I, Mahieu E, Chipperfield MP, Smale D, Hannigan JW, Friedrich M, Fraser P, Krummel P, Prignon M, Makkor J, Servais C, Robinson J (2022) Determination and analysis of time series of CFC-11 (CCl3F) from FTIR solar spectra, in situ observations, and model data in the past 20 years above Jungfraujoch (46°N), Lauder (45°S), and Cape Grim (40°S) stations. Environ Sci: Atmosheres 2:1487–1501

Perron P, Zhu X (2005) Structural breaks with deterministic and stochastic trends. J Econom 129(1):65–119. Modelling Structural Breaks

Proietti T (2000) Comparing seasonal components for structural time series models. Int J Forecast 16:247–260

Robinson PM (1989) Nonparametric estimation of time varying parameters. In: Hackl P (ed) Statistics, analysis and forecasting of economic structural change. Springer, Berlin

Szopa S, Naik V, Adhikary B, Artaxo P, Berntsen T, Collins W, Fuzzi S, Gallardo L, Kiendler-Scharr A, Klimont Z, Liao H, Unger N, Zanis P (2021) Short-lived climate forcers. Climate change 2021: the physical science basis. Contribution of working group I to the sixth assessment report of the intergovernmental panel on climate change. Cambridge University Press, Cambridge, United Kingdom and New York, NY, USA, pp 817–922

Vigouroux C, Stavrakou T, Whaley C, Dils B, Duflot V, Hermans C, Kumps N, Metzger J-M, Scolas F, Vanhaelewyn G, Müller J-F, Jones DBA, Li Q, De Mazière M (2012) FTIR time-series of biomass burning products (HCN, C_2H_6, C_2H_2, CH_3OH, and HCOOH) at Reunion Island (21° S, 55° E) and comparisons with model data. Atmos Chem Phys 12(21):10367–10385

Xiao Y, Logan J, Jacob D, Hudman R, Yantosca R, Blake D (2008) Global budget of ethane and regional constraints on U.S. sources. J Geophys Res 113:D21306

Yamanouchi S, Conway S, Strong K, Colebatch O, Lutsch E, Roche S, Taylor J, Whaley CH, Wiacek A (2023) Network for the detection of atmospheric composition change (NDACC) fourier transform infrared (FTIR) trace gas measurements at the University of Toronto atmospheric observatory from 2002 to 2020. Earth System Sci Data 15(8):3387–3418

Yurganov LN, Blumenstock T, Grechko EI, Hase F, Hyer EJ, Kasischke IS, Koike M, Kondo Y, Kramer I, Leung F-Y, Mahieu E, Mellqvist J, Notholt J, Novelli PC, Rinsland CP, Scheel HE, Schulz A, Strandberg A, Sussmann R, Tanimoto H, Velazco V, Zander R, Zhao Y (2004) A quantitative assessment of the 1998 carbon monoxide emission anomaly in the Northern Hemisphere based on total column and surface concentration measurements. J Geophys Res 109:D15305

Yurganov LN, Duchatelet P, Dzhola AV, Edwards DP, Hase F, Kramer I, Mahieu E, Mellqvist J, Notholt J, Novelli PC, Rockmann A, Scheel HE, Schneider M, Schulz A, Strandberg A, Sussmann R, Tanimoto H, Velazco V, Drummond JR, Gille JC (2005) Increased Northern Hemispheric carbon monoxide burden in the troposphere in 2002 and 2003 detected from the ground and from space. Atmos Chem Phys 5(2):563–573

Zander R, Mahieu E, Demoulin P, Duchatelet P, Roland G, Servais C, De Mazière M, Reimann S, Rinsland C (2008) Our changing atmosphere: evidence based on long-term infrared solar observations at the Jungfraujoch since 1950. Sci Total Environ 391(2–3):184–195

Zeng G, Wood SW, Morgenstern O, Jones NB, Robinson J, Smale D (2012) Trends and variations in CO, C_2H_6, and HCN in the Southern Hemisphere point to the declining anthropogenic emissions of CO and C_2H_6. Atmos Chem Phys 12(16):7543–7555

Zhang M, Vimont IJ, Jordaan SM, Hu L, McKain K, Crotwell M, Gaeta DC, Miller SM (2024) U.S. ethane emissions and trends estimated from atmospheric observations. Environ Sci & Technol 58(35):15539–15550. PMID: 39169712

Zhou M, Langerock B, Wang P, Vigouroux C, Ni Q, Hermans C, Dils B, Kumps N, Nan W, De Mazière M (2023) Understanding the variations and sources of CO, C_2H_2, C_2H_6, H_2CO, and HCN columns based on 3 years of new ground-based Fourier transform infrared measurements at Xianghe, China. Atmos Meas Techniques 16(2):273–293

Authors and Affiliations

Marina Friedrich[1,2] · **Siem Jan Koopman**[1,2] · **Yicong Lin**[1,2] · **Emmanuel Mahieu**[3] · **Stephan Smeekes**[4] · **Martine De Mazière**[5] · **Victoria Flood**[6] · **Matthias Max Frey**[7] · **Michel Grutter**[8] · **James W. Hannigan**[9] · **Frank Hase**[7] · **Nicholas Jones**[10] · **Rigel Kivi**[11] · **Maria Makarova**[12] · **Isamu Morino**[13] · **Isao Murata**[14] · **Tomoo Nagahama**[15] · **Justus Notholt**[16] · **Ivan Ortega**[9] · **Maxime Prignon**[17] · **Amelie Ninja Röhling**[7] · **Dan Smale**[18] · **Kimberly Strong**[6] · **Yao Té**[19] · **Minqiang Zhou**[20]

✉ Marina Friedrich
m.friedrich@vu.nl

Siem Jan Koopman
s.j.koopman@vu.nl

Yicong Lin
yc.lin@vu.nl

Emmanuel Mahieu
emmanuel.mahieu@uliege.be

Stephan Smeekes
s.smeekes@maastrichtuniversity.nl

Martine De Mazière
martine.demaziere@aeronomie.be

Victoria Flood
v.flood@utoronto.ca

Matthias Max Frey
matthias.frey@kit.edu

Michel Grutter
grutter@unam.mx

James W. Hannigan
jamesw@ucar.edu

Frank Hase
frank.hase@kit.edu

Nicholas Jones
njones@uow.edu.au

Rigel Kivi
rigel.kivi@fmi.fi

Maria Makarova
maria.makarova.spbu@gmail.com

Isamu Morino
morino@nies.go.jp

Isao Murata
imurata@tohoku.ac.jp

Tomoo Nagahama
nagahama@isee.nagoya-u.ac.jp

Justus Notholt
jnotholt@iup.physik.uni-bremen.de

Ivan Ortega
iortega@ucar.edu

Maxime Prignon
maxime.prignon@chalmers.se

Amelie Ninja Röhling
amelie.roehling@kit.edu

Dan Smale
dan.smale@niwa.co.nz

Kimberly Strong
strong@atmosp.physics.utoronto.ca

Yao Té
yao-veng.te@sorbonne-universite.fr

Minqiang Zhou
minqiang.zhou@mail.iap.ac.cn

[1] Department of Econometrics and Data Science, Vrije Universiteit Amsterdam, De Boelelaan, Amsterdam 1081HV, The Netherlands

[2] Tinbergen Institute, Valckenierstraat 59, Amsterdam 1018 XE, The Netherlands

[3] Department of Astrophysics, Geophysics and Oceanography, UR SPHERES, University of Liège, Quartier Agora, Liège 4000, Belgium

[4] Department of Quantitative Economics, Maastricht University, Minderbroedersberg, Maastricht 6211LK, The Netherlands

[5] Koninklijk Belgisch Instituut voor Ruimte-Aeronomie, Ringlaan, Ukkel 1180, Belgium

[6] Department of Physics, University of Toronto, St. George St, Toronto, Ontario ON M5S 1A7, Canada

[7] Institute of Meteorology and Climate Research Atmospheric Trace Gases and Remote Sensing, Karlsruhe Institute of Technology, 76131 Kaiserstr, Karlsruhe, Germany

[8] Instituto de Ciencias de la Atmósfera y Cambio Climático, Universidad Nacional Autónoma de Mexico, Av. Universidad, Mexico City 04510, Mexico

[9] Atmospheric Chemistry Observations & Modeling, NSF National Center for Atmospheric Research, 3450 Mitchell Lane, Boulder, CO 80301, USA

[10] School of Physics, University of Wollongong, Wollongong, NSW 2522, Australia

[11] Space and Earth Observation Centre, Finnish Meteorological Institute, Tähteläntie 62, Tähteläntie, Sodankylä 99600, Finland

[12] Department of Atmospheric Physics, St Petersburg State University, Ulyanovskaya St, Saint Petersburg 198504, Russia

[13] National Institute for Environmental Studies, Onogawa, Tsukuba 305-8506, Japan

[14] Graduate School of Environmental Studies, Tohoku University, Aramaki-Aoba, Sendai 980-8578, Japan

[15] Institute for Space-Earth Environmental Research, Nagoya University, Furocho, Nagoya 464-8601, Japan

[16] Institute of Environmental Physics, University of Bremen, 28359 Bibliothekstr, Bremen, Germany

[17] Department of Space, Earth and Environment, Chalmers University of Technology, Gothenburg 41296, Sweden

[18] National Institute of Water and Atmospheric Research, Becks-Lauder Road, Lauder 9377, New Zealand

[19] MONARIS (UMR8233), Sorbonne Université, Place Jussieu, Paris 75005, France

[20] State Key Laboratory of Atmospheric Environment and Extreme Meteorology, Institute of Atmospheric Physics, Chinese Academy of Sciences, Beichenxilu, Beijing 100029, China